SANDIA REPORT

SAND2014-18311
Unlimited Release
Printed September 2014

Reference Model 6 (RM6): Oscillating Wave Energy Converter

Diana Bull, Chris Smith, Dale Scott Jenne, Paul Jacob, Andrea Copping, Steve Willits, Arnold Fontaine, Dorian Brefort, Guild Copeland, Margaret Gordon, Rich Jepsen

Prepared by
Sandia National Laboratories
Albuquerque, New Mexico 87185 and Livermore, California 94550

Sandia National Laboratories is a multi-program laboratory managed and operated by Sandia Corporation, a wholly owned subsidiary of Lockheed Martin Corporation, for the U.S. Department of Energy's National Nuclear Security Administration under contract DE-AC04-94AL85000.

Issued by Sandia National Laboratories, operated for the United States Department of Energy by Sandia Corporation.

Available to DOE and DOE contractors from
U.S. Department of Energy
Office of Scientific and Technical Information
P.O. Box 62
Oak Ridge, TN 37831

Telephone: (865) 576-8401
Facsimile: (865) 576-5728
E-Mail: reports@adonis.osti.gov
Online ordering: http://www.osti.gov/bridge

Available to the public from
U.S. Department of Commerce
National Technical Information Service
5285 Port Royal Rd.
Springfield, VA 22161

Telephone: (800) 553-6847
Facsimile: (703) 605-6900
E-Mail: orders@ntis.fedworld.gov
Online order: http://www.ntis.gov/help/ordermethods.asp?loc=7-4-0#online

SAND2014-18311
Unlimited Release
Printed September 2014

Reference Model 6 (RM6): Oscillating Wave Energy Converter

Diana Bull, Guild Copeland, Rich Jepsen
Water Power Technologies
and
Margaret Gordon
Materials, Devices, and Energy Technologies
Sandia National Laboratories
P.O. Box 5800
Albuquerque, New Mexico 87185-MS1124

Chris Smith, Steve Willits, Arnold Fontaine
Applied Research Laboratory
Pennsylvania State University
PO Box 30
State College, PA16804-0030

Dale Scott Jenne
National Renewable Energy Laboratory
Wind and Water Power Program
15013 Denver West Parkway
Golden, CO 80401

Paul Jacob
Jacob Technologies
2703 Plantation Trail
Sugar Land, TX 77478

Andrea Copping
Pacific Northwest National Laboratories
902 Battelle Blvd.
Richland, WA 99354

Dorian Brefort
University of Michigan – Ann Arbor
500 S. State Str.
Ann Arbor, MI 48109

Abstract

This report is an addendum to SAND2013-9040: Methodology for Design and Economic Analysis of Marine Energy Conversion (MEC) Technologies. This report describes an Oscillating Water Column Wave Energy Converter reference model design in a complementary manner to Reference Models 1-4 contained in the above report.

In this report, a conceptual design for an Oscillating Water Column Wave Energy Converter (WEC) device appropriate for the modeled reference resource site was identified, and a detailed backward bent duct buoy (BBDB) device design was developed using a combination of numerical modeling tools and scaled physical models. Our team used the methodology in SAND2013-9040 for the economic analysis that included costs for designing, manufacturing, deploying, and operating commercial-scale MEC arrays, up to 100 devices. The methodology was applied to identify key cost drivers and to estimate levelized cost of energy (LCOE) for this RM6 Oscillating Water Column device in dollars per kilowatt-hour ($/kWh). Although many costs were difficult to estimate at this time due to the lack of operational experience, the main contribution of this work was to disseminate a detailed set of methodologies and models that allow for an initial cost analysis of this emerging technology.

This project is sponsored by the U.S. Department of Energy's (DOE) Wind and Water Power Technologies Program Office (WWPTO), within the Office of Energy Efficiency & Renewable Energy (EERE). Sandia National Laboratories, the lead in this effort, collaborated with partners from National Laboratories, industry, and universities to design and test this reference model.

ACKNOWLEDGMENTS

The authors would like to gratefully acknowledge the assistance of Dianne Murray (Sandia National Laboratory), who prepared technical illustrations for this report. Ann Dallman, who summarized the environmental compliance information provided by Pacific Northwest National Laboratory, and Vincent Neary, who reviewed and edited the final report.

The authors would like to acknowledge ReVision Consulting for the initial structural design of the BBDB.

The authors would like to acknowledge the Hydraulics and Maritime Research Center (HMRC) at University College Cork (UCC) for the testing time and expertise provided. In particular Brian Holmes, Brendan Cahill, and Florent Thiebaut were all heavily involved in executing the experimental testing of the BBDB device.

Diana Bull developed the power performance model for the BBDB and worked on many of the subsystem specifications as detailed below.

The Penn State team worked on the development of the power conversion chain for the BBDB in collaboration with Diana Bull.

Paul Jacob and Dorian Brefort worked on the mooring design for the BBDB in collaboration with Diana Bull.

D. Scott Jenne completed the economic modeling of the device.

Andrea Copping, Simon Geerloffs and Luke Hanna completed the environmental compliance analysis and environmental compliance costs of the design.

Guild Copeland and Rich Jepsen worked on the structural design first provided by Re Vision in collaboration with Diana Bull.

Jason Magalen of Sea Engineering, Inc. assisted Diana Bull in the SWAN modeling for the coastline.

Margaret Gordon worked to integrate all aspects of this reference model into a comprehensive report.

Contents

FIGURES

TABLES

NOMENCLATURE

AAP	average annual pneumatic (absorbed) power
AAEP	average annual electrical power
AAMP	average annual mechanical power
ASTM	American Society for Testing and Materials
BBDB	backward bent duct buoy
BEM	boundary element method
CapEx	capital expenditures
COB	center of buoyancy
COG	center of gravity
DNV	Det Norske Veritas
DOE	Department of Energy
EERE	Office of Energy Efficiency & Renewable Energy
ESA	Endangered Species Act
FSE	free surface elevation
HMRC	Hydraulics and Maritime Research Centre
JPD	joint probability distribution
LCOE	levelized cost of energy
M&D	manufacturing and deployment
MEC	marine energy conversion
MHK	marine and hydrokinetic
NDBC	National Data Buoy Center
NEPA	National Environmental Policy Act
NOAA	National Oceanic and Atmospheric Administration
O&M	operations and maintenance
OpEx	operational expenditures
OWC	oscillating water column
PCC	power conversion chain
PNNL	Pacific Northwest National Laboratory
PTO	power take off
RAO	response amplitude operator
RANS	Reynolds-averaged Navier Stokes
RM6	Reference Model 6
RMS	root mean square
RPM	revolutions per minute
SAEP	Significant Average Annual Electric Power
SNL	Sandia National Laboratories
TRL	Technology Readiness Level
WEC	wave energy converter
VFD	variable frequency drive

1 REFERENCE MODEL 6 (RM6): OSCILLATING WAVE ENERGY CONVERTER

1.1 RM6 Description

Reference Model 6 (RM6) is a Backward Bent Duct Buoy (BBDB), which is a type of oscillating water column wave energy converter. First proposed by Masuda[1], the BBDB design is a floating Oscillating Water Column (OWC) device that consists of an air chamber, an L-shaped duct, bow and stern buoyancy modules, and a power take-off (PTO) composed of a Wells air turbine and a generator as shown in Figure 1-1. This L- shaped device opens to the ocean downstream from the wave propagation direction. Power is produced by the motion of the wave, which causes the ambient pressure in the air chamber to vary thereby forcing air to flow through the Wells turbine. Figure 1-1 illustrates the main components and dimensions of a BBDB.[2] This design was engineered to withstand the hydrostatic pressure at a submergence of up to 25 m.

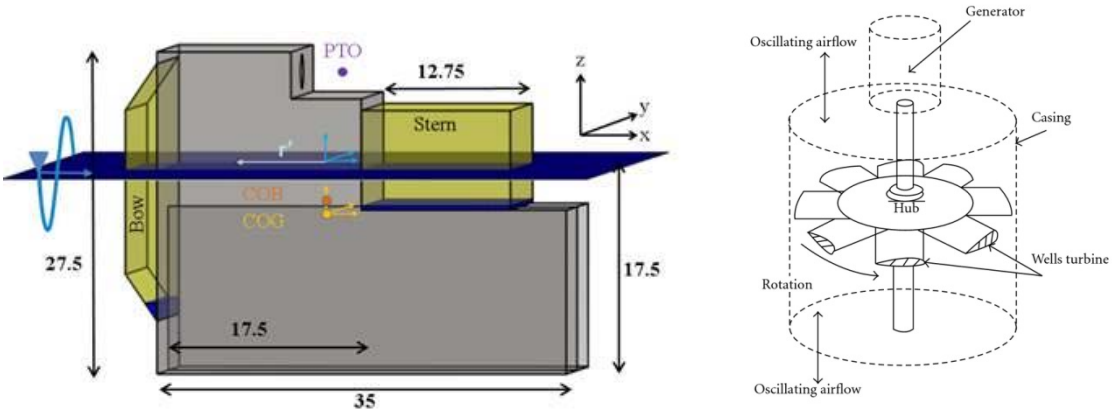

Figure 1-1: RM6 BBDB Device Design and Dimensions and Wells Turbine schematic. The width of the device (not shown) is 27 m.

The floating BBDB design capitalizes on the coupling between the motion of the structure and motion of the free surface contained within the structure. This coupling can expand the frequency range over which good power conversion occurs thus yielding a higher primary conversion efficiency when compared to other OWC's.[2]

1.1.1 Device Design and Analysis

As noted in Design Methodology for a Single Device, Section 2.1.1,[3] the first step in the device design process was to develop a conceptual design for a Wave Energy Converter (WEC) device appropriate for the modeled reference resource site. Once the concept design was completed, a detailed device design, as described in Section 1.3 below, was developed using a combination of numerical modeling tools and testing scaled physical models. More detailed descriptions of the structural device design and analysis are provided in the 2014 SAND report by Copeland, Bull, and Jepsen.[4] Mooring and anchoring design and sensitivity analysis details can be found in [5] and [6]. Complete details of the wave-to-pneumatic performance of the BBDB are described in two references: a EWTEC 2013 conference paper that describes the

monochromatic performance model,[2] and a METS 2014 conference publication on the random wave performance of the BBDB.[7] Experimental verification work was completed at the Hydraulic Maritime Research Center (HMRC) housed at the University College Cork (UCC) and an overview of this work can be found in the 2014 SAND report.[8] Details on the design of the power conversion chain (PCC) can be found in an abbreviated form in a METS 2014 paper,[9] and in more complete form in the 2014 SAND report.[10]

1.2 Module Inputs

1.2.1 Site Information

The reference wave energy resource for RM6 was developed from site information collected near Eureka, in Humboldt County, California. This wave energy site has a wave climate that is representative of the west coast of the United States. The reference site was identified as a promising future deployment site and a wealth of met-ocean data is available for accurately characterizing its wave energy resource. The Eureka coast reference site was also the proposed site for Pacific Gas & Electric's WaveConnect™ pilot project test bed.[11]

1.2.1.1 Bathymetry and Bed Sediments

As shown in Figure 1-2 the deployment site features a gently sloping seabed without many irregularities (such as the canyons located farther to the south) that could disturb the local wave field. It is therefore likely that the wave-field is homogeneous over the deployment area of interest. The RM6 BBDB wave energy converter was designed for deep-water deployment, where the water depth is in the range between 40 m and 100 m.

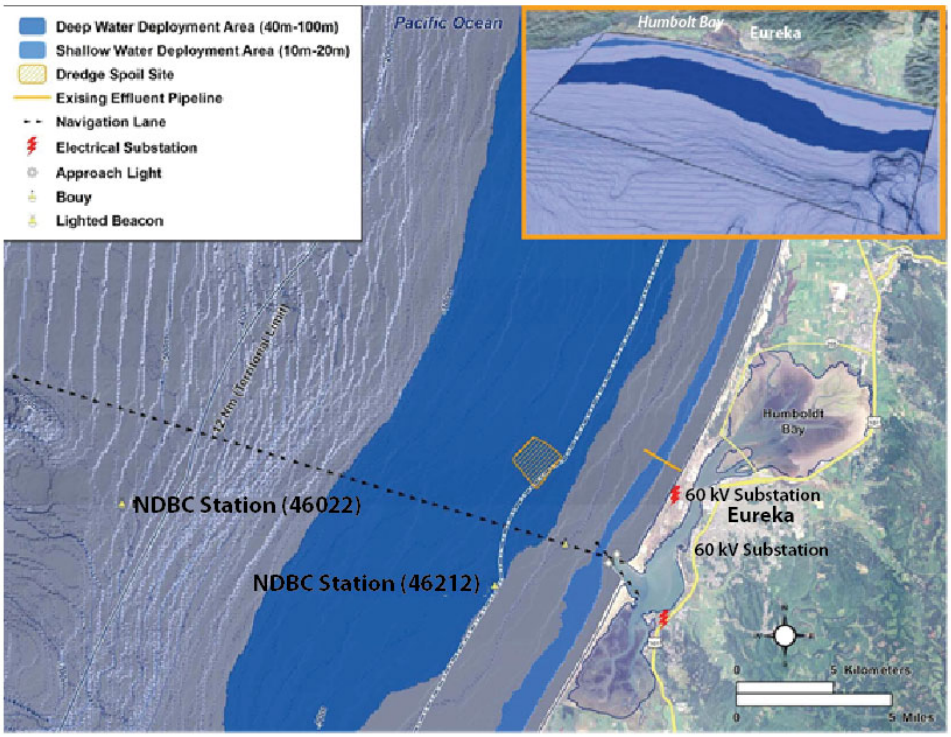

Figure 1-2: Local site bathymetry plan and reference site grid interconnection options.

Sediment classification enabled a detailed seabed characterization at the reference site, which is a sedimentary shelf throughout the deep-water deployment zone. This information is also very important to assess the impacts that the RM6 device and array will have on the marine environment and ecosystem. Most of the seabed in the near shore region of the Humboldt site consists of soft sediments (sand and clay). There are rocky areas near Trinidad Head to the

north, but these areas can be avoided. Sediments within the proposed cable route and deployment area are well suited for subsea cable burial and anchoring.

1.2.1.2 Operational Wave Characteristics

According to linear wave theory, the wave energy flux for irregular waves in deep water is

$$J_s = \frac{\rho g^2}{64\pi} H_s^2 T_e \qquad 1$$

where J_s is the wave energy flux per unit of wave-crest length for irregular waves, H_s is the significant wave height, T_e is the wave energy period, ρ is the water density, and g is the acceleration of gravity. Based on Eq.1, more wave power is available when the wave height is larger and the wave period is longer. The BBDB is asymmetric and as such will absorb varying amounts of power depending upon the incident direction. The Eureka climate has a stable wave direction for operational waves and hence the analysis presented in this report assumes the waves are uni-directional and perpendicular to the forward facing float.

The operational characteristics of the Northern California wave climate can be represented in terms of the joint probability distribution (JPD) of sea states. The JPD indicates the frequency of occurrence of a given sea state, defined by a significant wave height and wave energy period pair, that occurs any given year. The reference BBDB model was designed to operate in a near shore Northern California environment. The JPD for the reference site is shown in Table 1-1.[9] The deployment site is approximately 3 miles from shore on a 60 m depth contour off the Northern California coast near Eureka. Archived summary statistics from National Data Buoy Center (NDBC) 46212 buoy were used to generate the JPD of significant wave height with peak period T_p. This data buoy is located in 40 m of water depth. Summary statistics spanning seven years (2004-2011) were used for this analysis. Although this data buoy has recorded the directional spectrums, only the significant wave height and peak period are used to characterize the deployment location. Table 1-1 shows the 46212 JPD; the sum of all values within the JPD is one, which represents 100% of all sea states. The JPD is presented such that important aspects of the wave climate may be quickly assessed. For example, 95% of the time the wave climate is within the pink boxes, 75% of the time it is in the yellow boxes, and 50% of the time within the green boxes. The red highlighted values indicate the most common period for each *Hs*. The bold red value (0.046 or 4.6%) indicates the most commonly occurring sea state. It is clear from the shapes moving from 95% to 75% to 50% that the deployment location is predominantly a mixture of shorter wind waves and longer swell waves.

Table 1-1: Wave statistics data for reference resource. Total incident wave power flux: 37.4 kW/m.

Significant Wave Height, Hs [m] \ Peak Period, Tp [sec]	4.7	5.7	6.7	7.7	8.7	9.7	10.7	11.7	12.7	13.7	14.7	15.7	16.7	17.7	18.7
0.25	0.0	0.0	0.0	0.0	0.0	0.0	0.0	0.0	0.0	0.0	0.0	0.0	0.0	0.0	0.0
0.75	0.0	0.004	0.011	0.011	0.013	0.004	0.006	0.003	0.0	0.0	0.003	0.004	0.005	0.0	0.0
1.25	0.0	0.010	0.028	0.024	**0.046**	0.018	0.022	0.011	0.009	0.007	0.005	0.004	0.004	0.002	0.0
1.75	0.0	0.002	0.025	0.027	0.036	0.021	0.035	0.019	0.014	0.012	0.010	0.005	0.005	0.003	0.0
2.25	0.0	0.0	0.006	0.023	0.036	0.017	0.033	0.024	0.019	0.015	0.010	0.006	0.005	0.003	0.0
2.75	0.0	0.0	0.0	0.009	0.027	0.010	0.022	0.020	0.015	0.013	0.009	0.005	0.005	0.003	0.0
3.25	0.0	0.0	0.0	0.0	0.011	0.007	0.012	0.013	0.012	0.011	0.008	0.005	0.004	0.0	0.0
3.75	0.0	0.0	0.0	0.0	0.003	0.003	0.005	0.007	0.007	0.007	0.006	0.003	0.003	0.0	0.0
4.25	0.0	0.0	0.0	0.0	0.0	0.0	0.0	0.003	0.003	0.004	0.004	0.0	0.002	0.0	0.0
4.75	0.0	0.0	0.0	0.0	0.0	0.0	0.0	0.0	0.0	0.0	0.002	0.0	0.0	0.0	0.0
5.25	0.0	0.0	0.0	0.0	0.0	0.0	0.0	0.0	0.0	0.0	0.0	0.0	0.0	0.0	0.0
	4.0	4.9	5.7	6.6	7.5	8.3	9.2	10.0	10.9	11.7	12.6	13.5	14.3	15.2	16.0

Energy Period, Te [sec] $2\pi(m_{-1}/m_0)$

NOTE: H_S = significant wave height; T_e = wave energy period.

1.2.1.3 Extreme Sea States

The reference BBDB model was designed to withstand extreme sea states native to the Northern California deployment site. Data for extreme sea states during storms was evaluated using 10 National Data Buoy Center (NDBC) buoys located near Eureka, CA off the west coast of the U.S. (red labels in Figure 1-3).

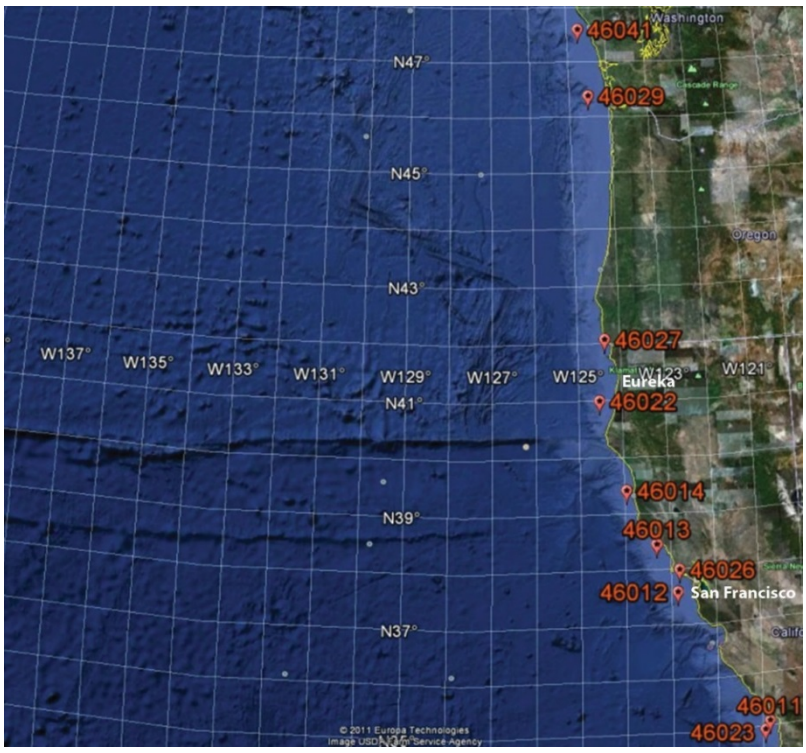

Figure 1-3: NDBC buoy locations for extreme wave measurements.

At these measurement locations, a typical 100-year significant wave height during storms is generally in the range between 8 m and 13 m. Specific extreme wave conditions during storms near Humboldt site (station 46022) were described by Berg (2011),[12] where the 100-year return period significant wave height was estimated to be between 11 m and 12 m, and the peak wave period was estimated at 17 sec. The values were then used as a guide to determine the extreme wave loads in OrcaFlex.

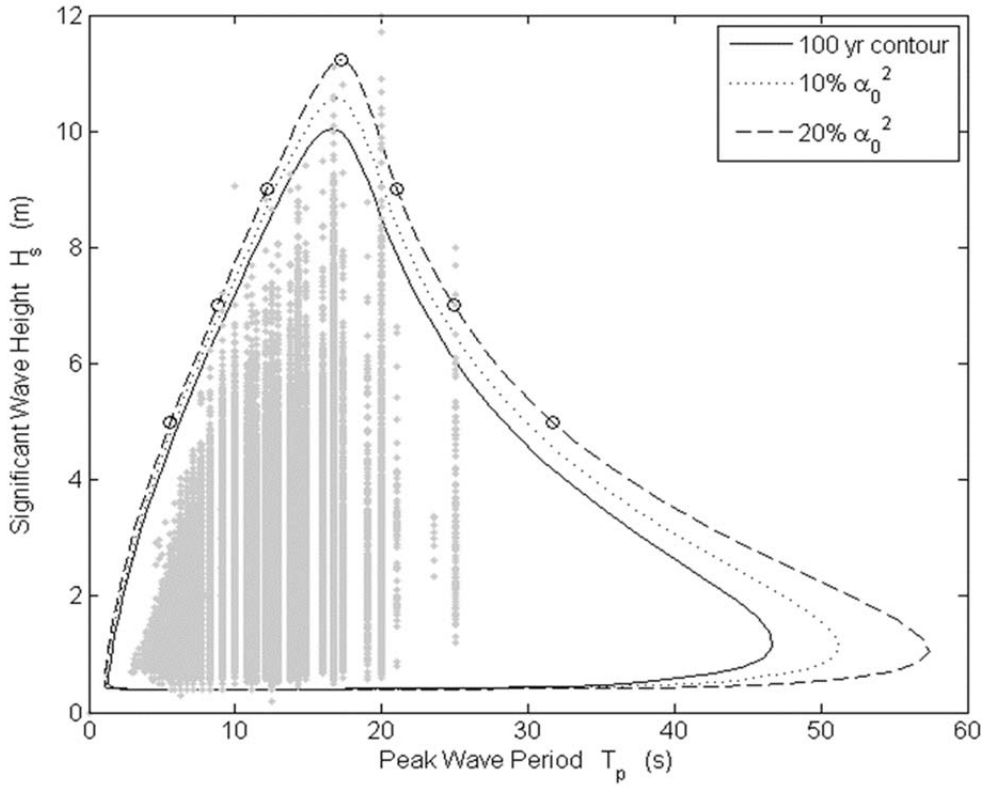

Figure 1-4: 100-year contour for NDBC buoy 46022 (Berg 2011).

As recommended by DNV rules,[13] the extreme environment was assumed to consist of collinear waves, current, and wind. Hence, the results from the 100-year contour were then combined with the wind and current profiles to represent the survival condition for the BBDB. This data is summarized in Table 1-2.[12]

Table 1-2: Severe Weather Characteristics at Reference Site, assuming 600 m depth waves

	Depth	600 m
Spectral Parameters	Significant Wave Height	11.22 m
	Peak Period	17.26 sec
	Spectrum	JONSWAP or Bretschneider
Sinusoid Equivalent	Equivalent Wave Height	21.3 m
	Period	17 sec
	Wave Type	5th order Dean Stream
Wind Profile	100 yr. Wind at 10[m] above SWL	29.6 m/s
	Wind Profile	constant
Current Profile	10yr Surface Current	0.33 m/s
	Current Profile	linear decrease to zero

This data was derived from a wave-rider buoy located at a depth of approximately 600 m, and is conservative for two reasons. First, the wave height shown here is higher than for a 60 m depth in which the device will be located. Second, in the 60 m depth case, waves will be refracting to align themselves perpendicular to shore. Hence as opposed to sizing the mooring for an incident direction along one leg, the storm will likely hit the device between the starboard and port legs thus decreasing the load that any one leg must resist.

Predicted sea states using the wave model SWAN,[14] summarized in Table 1-3, shows wave height differences between a 600 m depth and a 40 m depth. We can see that the regular wave equivalent height of the 40 m depth is 3.5 meters lower than that of the 600 m depth. The BBDB device will operate in a water depth of 60 m, so we can expect storm condition regular wave equivalent heights close to 18 meters as opposed to 22 m.

Data on the directionality of storm waves is shown in Figure 1-5. Notice that for a 40 m depth, storm wave incident direction is a lot more peaked than for the 600 m depth case. Furthermore, at 40 m depths, storm direction is very close to the operational waves.

Table 1-3: Wave Characteristics at 630 and 40 m Depths

SWAN Results for Storm Waves Propagating from a 630 m Depth to a 40 m Depth				
		Storms at ~600 m Depth	Southern Storm at 40 m Depth	Northern Storm at 40 m Depth
Spectral Wave Data	Significant Wave Height	11.22 m	9.39 m	9.35 m
	Peak Period	17.26 sec	17.13 sec	17.13 sec
	Incident Direction	243 degrees	273 degrees	318 degrees
	Spectrum	JONSWAP or Bretschneider	JONSWAP or Bretschneider	JONSWAP or Bretschneider
Regular Wave Data				
	Equivalent Height	21.32 m	17.84 m	17.77 m
	Period	17 sec	17 sec	17 sec
	Wave Type	5th order Dean Stream	5th order Dean Stream	5th order Dean Stream

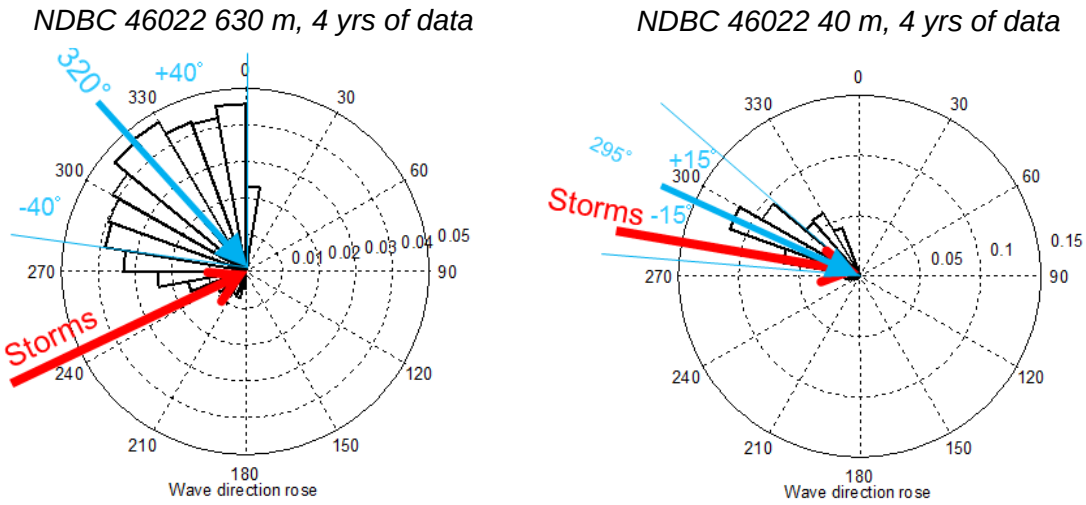

Figure 1-5: Operational and Storm Wave Directionality at 630 and 40 m Depths

1.2.1.4 Adjacent Port Facilities and Grid Options

Figure 1-6 shows a nautical chart of the Humboldt Bay area of interest. The port nearest to the area is located within Humboldt Bay and serves as the only deep-water port on California's North Coast. The facilities are well suited for installation and operational activities that would be required by nearby wave farms. Multiple piers within the bay would also greatly facilitate the launching of any WEC installation project and provide some of the necessary infrastructure for operational activities.

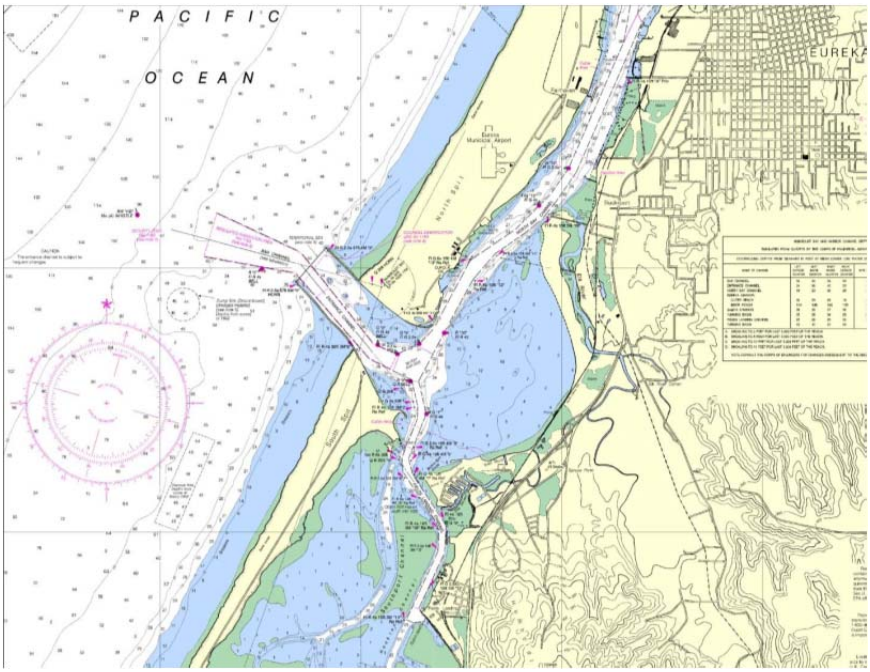

Figure 1-6: NOAA nautical chart (Humboldt Bay).

Approximately 5 miles north of the Humboldt Bay inlet, there is a 60 kV substation in very close proximity to the coastline. This station would serve as the interconnection point to the local electrical grid. An existing outfall location (orange line shown in Figure 1-2) could be used to accommodate the proposed electrical subsea cable and eliminate the need to directionally drill to shore to accommodate the power cable landing. However, this option was not considered for estimating installation costs in this study.

1.2.2 Device /Array Information

In the conceptual design, we determined design specifications based on site resource characteristics borrowed from successful commercial technologies and by applying engineering judgment, economic considerations, and simple hand calculations. A summary of the design specifications is given in Table 1-4.

Table 1-4: RM6 Design Summary

Category	Description	Specification	Justification	Details
Environment	Operational Depth	Water depth 60 m	Site resource characteristics	Sufficient depth for deep-water WEC design.
	Directionality	Refer to Figure 1-5		Assuming uni-direction seas in power performance calculations
	Operational sea states	T_e=5sec~18sec; H_s=0.75m~6m 37.4 kW/m incident wave power flux	Site resource characteristics	Based on the wave statistic data (JPD) at the reference site
	JPD	In Table 1.1		
Device	WEC Type	Oscillating Water Column	WEC architecture	Backward Bent Duct Buoy (BBDB) Floating Oscillating Water Column
	Mooring	3-mooring slack line design	Standard design for floating WECs	Designed for mooring loads under extreme 100-year return period sea state.
	Power Conversion Chain	Fixed Pitch Wells Turbine coupled to a Generator and Variable Frequency Drive	Required a linear relationship between pressure and flow as well as the ability to adjust resistive loading as a function of sea state	Turbine tip radius: 1.588 m Generator rating: 298 kW VFD rating (variable frequency drive): 373 kW
Performance	Absorbed Power		208kW	This is the average annual value
	Mechanical Power	Includes losses of turbine	118 kW	This is the average annual value
	Electrical Power	Includes losses of generator and VFD	103 kW	This is the average annual value
Deployment	Array configuration	Staggered with 30 float diameter separation	Literature. Engineering judgment.	Avoid device interaction according to Babarit (2012).[15]
	Array requirements	Sufficient space to accommodate mooring connections and device watch circle.	Literature. Engineering judgment.	Avoid device interaction according to Babarit (2012).[15]

1.3 Device Design, Performance and Analysis

1.3.1 Structural Design

WEC devices must be designed to sustain the extreme sea states during severe storms. This section discusses two structural designs (a detailed design and a more simplified version) and stress analysis of the RM 6 Oscillating Water Column device. [4]

The majority of the device dimensions were selected based upon the conclusions of the following papers[16], [17], and [18]. This design profile is not optimized to reduce viscous losses or encourage weathervaning as is depicted in [19] and [20].

1.3.1.1 Detailed Structural Dimensions and Geometry Design

A detailed BBDB model was designed by Re Vision Consulting which included the load and structure calculations (design pressure, stiffener spacing, and stiffener and girder sizing) for the BBDB WEC.[4] Ideally, the structure would be designed to withstand the dynamic loading that would occur in an extreme environment. This dynamic loading would be a combination of nonlinear dynamic pressure, green water (water on top of the structure), and/or slam loads from waves crashing on top of the structure or the structure hitting the surface of the water. However, all of these loads are highly nonlinear, and the tools to assess these loads [e.g., Reynolds-averaged Navier-Stokes (RANS) solvers, LAMP, AEGIR] are beyond the scope of the Reference Model project. Therefore, the design load was estimated conservatively and used to generate the structure specifications. It is recognized that these calculations yield a single non-optimized possible design for the structure of a BBDB. Given the conservative estimate of the design load, the BBDB WEC design is not the most economical or efficient.

1.3.1.1.1 Design Pressure Calculations

Without using tools able to assess non-linear dynamic loads or experimental data, a design load had to be estimated in order to substantiate a realistic structural design. Hence, a design load was assumed that corresponded to the hydrostatic pressure with a green water depth of 6.0 m. This green water depth is applied to the entire structure and the lowest point is used to uniformly design the structural requirements. Eq.'s 2 and 3 below more fully describe the calculation of this design load.

$$D = dd + dg = 17.5\,\text{m} + 6.0\,\text{m} = 23.5\text{m} \quad (2)$$

Where *D* is the design depth, *dd* is the maximum device draft and *dg* is the green water depth. The design depth is then used in the calculation of the design pressure as shown below:

$$DP = D * \rho * g = 23.5\,\text{m} * 10.25\frac{\text{kg}}{\text{m}^3} * 9.81\frac{\text{m}}{\text{s}^2} = 236300\frac{\text{N}}{\text{m}^2}. \quad (3)$$

Where *DP* is the Design Pressure, ρ is the density of sea water and *g* is the gravitational constant. Although simplistic, this severe hydrostatic loading should be conservative enough to account for the dynamic loading expected in extreme events.

1.3.1.1.1.1 Stiffener and Girder Specifications

With an estimate of the design pressure, Re Vision was then able to use the Det Norske Veritas (DNV) Rules for Classification of Ships: Hull Structural Design, Ships with Length Less Than 100 Meters, Part 3[21], to specify the correct relationship between plate thickness and stiffener

spacing.[4]A structure must be stiffened both vertically and horizontally. There are distinct stiffening elements referred to as stiffeners and girders. Girders typically have a T-shaped cross-section and are the main horizontal and vertical support for a structure. The stiffeners are smaller in dimension and act locally as support between the girders. Figure 1-7 illustrates the Re Vision design. The Re Vision design uses T-shaped girders which are approximately 0.4 x 0.4 m and have a cross sectional area of 0.032 m^2. The Re Vision design uses stiffeners that are L-shaped and approximately 0.1 x 0.2 m with a cross sectional area of 0.0048 m^2.

Re Vision used ASTM A36 steel (36 ksi yield strength) for its model. The calculated parameters are listed in Table 1-5.

Table 1-5: Plate, Stiffener and Girder specifications

Plate thickness	15.875 mm
Stiffener Size (length)	1.97 M
Stiffener Spacing	0.75 M
Girder Size (length)	4.5 M
Girder Spacing	1.97 M

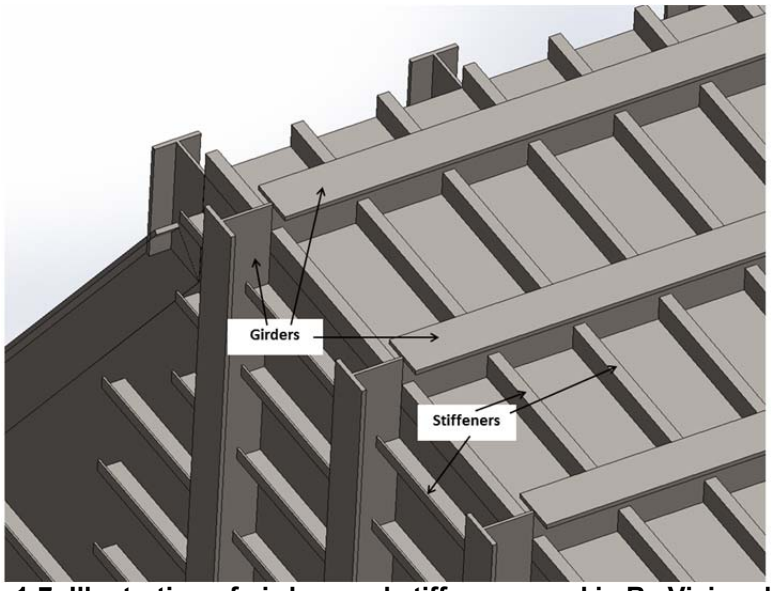

Figure 1-7: Illustration of girders and stiffeners used in Re Vision design.

1.3.1.1.1.2 Mooring Loads Analysis and Structural Modifications

In addition to loads arising from hydrodynamic pressure, analysis of the structural requirements to withstand the load presented by the mooring attachment points was also performed. Complete details may be found in [4]. Mooring design is discussed below in section 1.3.2. However, for clarity, the configuration is presented here.

The mooring loads were determined by Sandia with a three line configuration and using OrcaFlex in extreme wave conditions for survival loads. Figure 1-8 shows the mooring line configuration in plan view as modeled in OrcaFlex. Attachment points were placed at 8.75 m above the bottom of the structure for the OrcaFlex analysis. This provided the maximum load

and direction in which the mooring lines would act on the OWC structure.

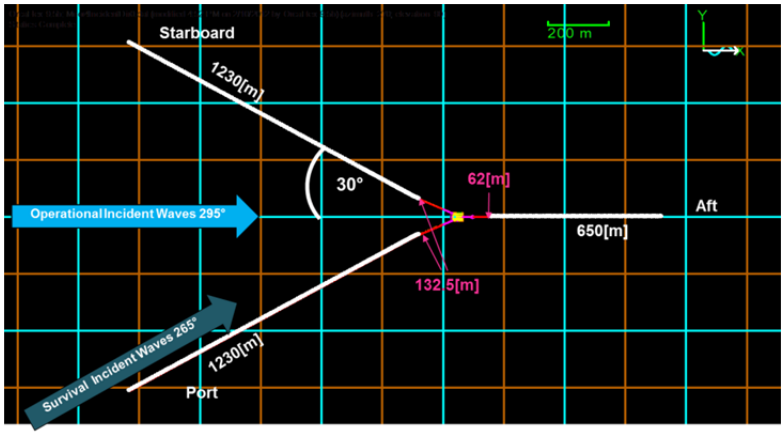

Figure 1-8: Plan view of mooring line configuration in OrcaFlex

The maximum tension load of 2318 kN was found affecting the port side attachment at near 90 degrees. The plate supporting this attachment was shown to be insufficient in size or material strength to withstand this maximum load. Therefore, supporting plates as shown in Figure 1-9 were added to the buoyancy chamber plate with geometry similar to the load spreading that resulted from the preliminary simulations in which the plate failed.

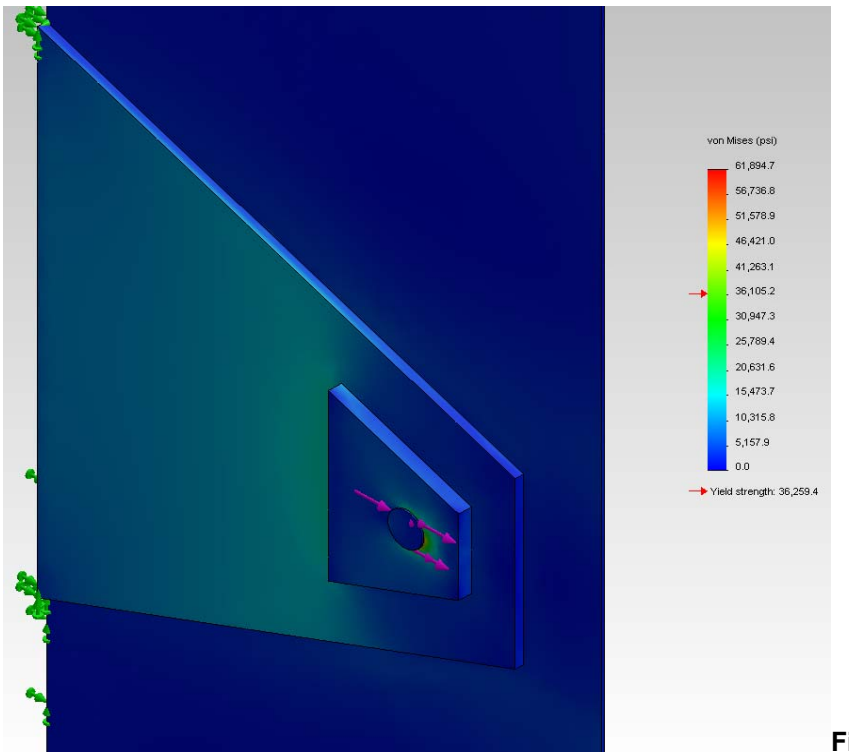

Figure 1-9: Additional plate to support the maximum mooring load (2320 kN). Attachment point is shown

The simulation was done using Solidworks Simulation static analysis with a peg inserted into the attachment hole with no contact defined. The mooring load was applied as a bearing load in the

attachment point. The back and top edges of the buoyancy chamber plate were fixed. Please refer to the report by Copeland, Bull, and Jepsen[4] for complete simulation details.

The results of the simulation demonstrated that the intermediate support plate had stresses less than half of the yield strength and provided the necessary factor of safety of at least 1.5. However, there are stress concentrations on the outer support plate along the concentric edge in which the load is applied that are near 60 ksi. The use of steel with a material strength significantly greater than the A36 steel used elsewhere in the design of the OWC was identified as the sole method to accommodate this stress. The results show that 120 ksi steel would be sufficient in this application. Since the outer most plate is quite small compared to the rest of the OWC structure, it is reasonable to modify the material at this location only to survive the larger mooring load applied at this point. It should also be noted that steel typically used in rigging and mooring applications (shackles, bolts, etc.) is 180 ksi in yield strength.

The maximum mooring loads at the aft location are almost half of that for the port side. Model simulations show that only the smaller, 120 ksi support plate is necessary to withstand the maximum load.

The installation of these plates would be inserted into cut-out sections of the hull plates such that through welds are achievable and the support plates spread the load throughout their volume and not just along the edges. The plates cannot be simply placed on top of the existing hull plates and welded along the edges as the loads at the welds would be above their yield strength.

1.3.1.1.2 Detailed Structural Design Remarks

As stated above, these calculations are able to yield an estimate of how the structure could be built. Re Vision used the calculations detailed above to produce a SolidWorks model from which physical characteristics could be computed including total weight, center of gravity, centers of inertia and reserve buoyancy. Figure 1-10 in the next section illustrates the structural model that Re Vision designed. This original model was created as a single SolidWorks part hence making alterations to the design difficult.

The applicability of the chosen design pressure and the DNV standards to this particular design are not well understood. The design pressure was applied to the entirety of the structure as opposed to applying distinct pressure regimes to distinct areas. Previous work[4] has indicated that the dynamic pressure could be a factor of 10 to 100 less than the hydrostatic submergence predicted in Eq. 3.[3] A change of this scale for the design condition would dramatically alter the recommended design. Since the design needed little alteration to handle the loads at the mooring connection points, it is likely that the hydrostatic design pressure is a much more conservative estimate than should be realistically applied. Additionally, the motivation for the plate thickness selected by Re Vision was not explicitly stated and hence, this applicability of this choice is also not fully understood.

Thus, although a design is presented here, this design is not promoted as the most economical or efficient. It is intended to be conservative and to highlight the beginning steps one would take to

design a WEC structure. It is known that this reference device is much heavier than commercial analogs (i.e. Ocean Energy Ltd.[19]).

1.3.1.2 Simplified Structural Design Model

A new model was created by SNL in order to represent the structure in a simple modular fashion so that alterations of the buoyancy chambers could be implemented and the analysis of the resulting changes in buoyancy would be uncomplicated. The first step was to replace the original OWC model which was created as a single SolidWorks part with a simplified SolidWorks assembly that would have equivalent mass and centers of gravity and buoyancy. Part of this simplification was to replace the original structure's plates, girders and stiffeners with a basic plate-only construction that had an equivalent mass. The approach was to use stainless steel plate for the model and adjust the thickness of this plate to give the same mass per unit surface area as the original plate/girder/ stiffener construction. The Duct bulkhead was modeled separately. The SAND report[4] contains the complete calculation details that are not presented here. The plate thicknesses are presented in Table 1-6.

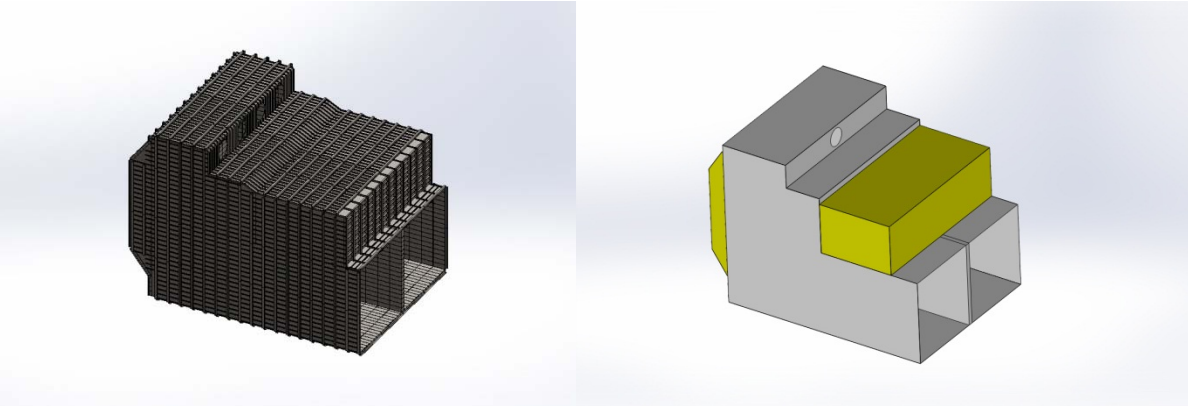

Figure 1-10: Original Model **New Model**

Table 1-6: Simplified model structural specifications

Stainless Steel	ASTM A36 Steel
Plate thickness (Duct Bulkhead)	0.0467 M
Plate Thickness (rest of device structure)	0.0351 M

1.3.1.3 Final BBDB Structural Design Specifications

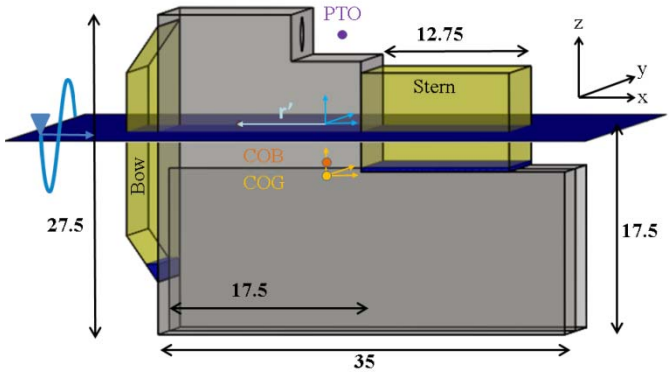

Figure 1-11: Model of the OWC describing dimensions, locations of principal components, locations of the COB and COG, and identifying coordinate systems

The structural design assumes a uniform thickness of A36 steel, appropriate ballast mass and placement, and an estimate of the mass and location of the power conversion chain. An average wall thickness of 35.1 mm is applied to the entire device. This average thickness was derived from a structural design engineered to withstand the hydrostatic pressure at a submergence of 25 m. The ballast is distributed to obtain the desired draft and ensure that the center of gravity and the center of buoyancy are aligned vertically. The ballast is assumed to be seawater and is added to the buoyancy chambers as shown in Figure 1-11. The mass of the power conversion chain (drivetrain, generator, power conditioning electronics) is approximated and is placed at the expected center of the Wells Turbine location, also shown in Figure 1-11. Table 1-7 summarizes the structural properties of the device that are needed as input into WAMIT.[22]

Table 1-7: Structural properties of the BBDB device

Displaced Mass [kg]		2,024,657		
Structural Mass [kg]		1,808,944		
Bow Ballast Mass [kg]		22,072		
Stern Ballast Mass [kg]		123,641		
Power Conversion Mass [kg]		70,000		
COG (x,y,z) [m]		0.00	0.00	-4.29
COB (x,y,z) [m]		0.00	0.00	-3.31
Free Surface Center (x,y,z) [m]		-5.12	0.00	0.00
Radius of Gyration at COG [m]	x	12.53	0.00	0.00
	y	0.00	14.33	0.00
	z	0.00	0.00	14.54

Table 1-8: Key properties of the BBDB

	BBDB
Equilibrium Entrained Water Mass	15,255,844
Length of Water Column [m]	35
Surface Area of Water Column [m^2]	473
Heave Natural Period [sec]	16.1
Pitch Natural Period [sec]	11.6
Coupled OWC Natural Period [sec]	8.61

1.3.2 Foundation and Mooring

Two publications detail the mooring and anchoring design of the BBDB. The first was presented at Oceans 2012[5] and it details the methodology of building an OrcaFlex model. The second is a SAND report[6] detailing the sensitivity analyses performed on the final mooring and anchoring design. These references are summarized here; more detailed explanations can be found in either of these papers.

1.3.2.1 Foundation and Mooring Design

The cost of a Wave Energy Converter (WEC) mooring system is a significant portion of the total installed cost of a WEC device.[23] The mooring system specifications are driven by the extreme sea states. Consequently, it is important to obtain realistic load predictions early in the design process so that mooring system components can be realistically sized. It is also important that the design procedure for the mooring system be easily adaptable so that mooring configurations can be modified and updated without major time and expense.

1.3.2.1.1 Model Simulations

During severe weather conditions, the device's diffraction parameter is small and its wave height to characteristic length ratio is large; therefore, the hydrodynamic forces on the device can be calculated using Morison's Equation.[5] This allows for the use of OrcaFlex, a time domain mooring line dynamics software, to analyze the performance of the BBDB's mooring system.

To do this analysis in OrcaFlex, a model of the BBDB OWC was developed using an array of 6-DOF lumped bodies representing:

- buoyancy distribution,
- freely flooding bodies that account for the time-dependent variation of entrained water mass, and
- hydrodynamic characteristics that account for inertial and viscous effects.

The mooring layout was designed to maximize energy production in the operational climate but still have high reliability in severe weather conditions at the chosen test site near Eureka, CA. Therefore, the mooring was laid out to have two front lines separated by 60º with the bisector of that angle being the operational incident wave direction and the aft line along the operational incident wave direction. Wave incident direction during severe weather conditions mostly comes from a ±30º direction from the operational wave direction as shown in Figure 1-5. Hence, the majority of the storm load will affect one mooring leg. A layout of the mooring system used to determine the mooring specifications is shown in Figure 1-12.

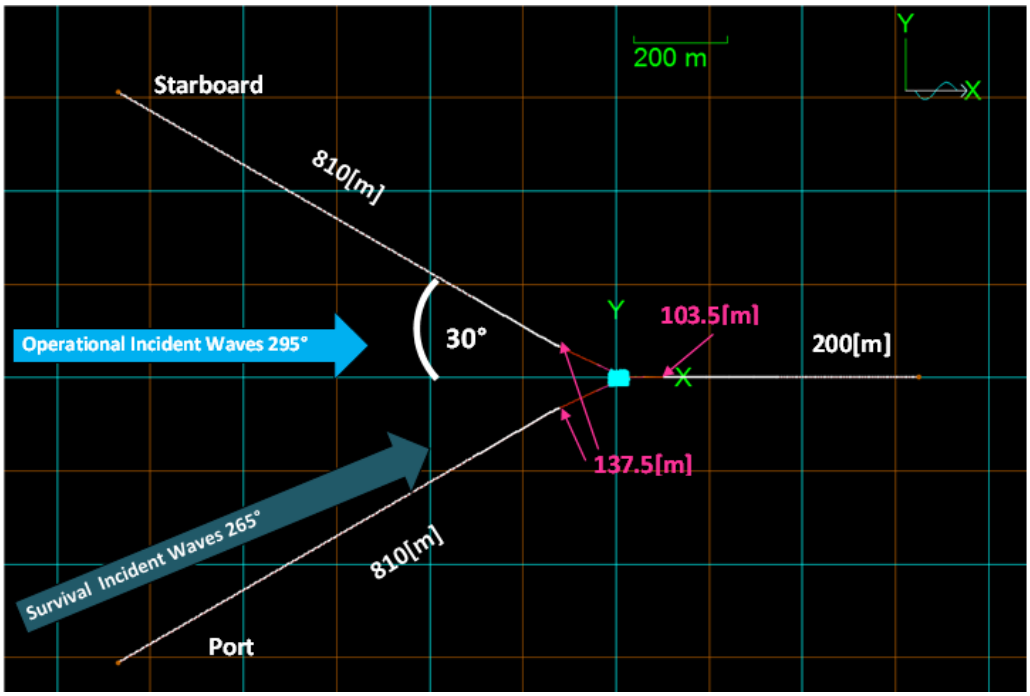

Figure 1-12: Reference Model Mooring Layout

Severe weather analysis was performed under a variety of conditions which are described in Table 1-2. As recommended by DNV rules,[13] the extreme environment was assumed to consist of collinear waves, current, and wind. Severe weather simulations were run by setting the extreme weather incident direction collinear with the port mooring line to evaluate the maximum load that it would experience and size the forward mooring lines appropriately.

1.3.2.1.2 Simulation Remarks

The simulation results are able to yield the specifications that the mooring and anchoring system must meet. However, these simulations are sensitive not only to the environmental input (as mentioned in Section 1.2.1.3) but also to the model inputs (the hydrodynamic characteristics). Hence a study was completed to assess the sensitivity of the mooring specifications to the incident wave direction and the magnitude of the viscous losses.[6] As will be shown below, although the environment that was used to specify the mooring and anchoring may be conservative, the values used in the OrcaFlex model to specify the hydrodynamic characteristics may not be conservative.

1.3.2.1.2.1 Directional Study

Storm waves will never be entirely uni-directional, but at the chosen test site near Eureka, CA, it is known that storm waves mainly come at an angle between 0 and 30 degrees to the port side from the operational wave direction, as described in section 1.2.1.3 and Figure 1-5. As expected, the peak loads on the mooring lines and anchors shift from both front mooring lines, to primarily the port line as the incident direction changes from 0 to 30 degrees (see Table 1-9, the green shading indicates all loads below failure). As shown in the report[6] the factor of safety on the mooring line specification changes from 1.65 for the 30 degree case to 2 for the 0 degree case whereas the anchor factor of safety changes from 1.5 to 1.93. In addition, since the deployment

location has only 60m of water depth, the storms are expected to be incident from 0 degrees. This would incur a more balanced load, hence smaller lines and anchors could have been chosen.

Although a similar study was not performed altering the wave height, previous results in SWAN have shown that at a shallower depth, the wave height of the storm will be lower. From 600 m depth to 40 m depth, the wave height was found to drop from a H_s of 11.22 m to 9.39 m. The results discussed above are calculated for the 600 m depth wave, while the deployment site has a 60 m depth. Also, at 60 m of depth, the waves will have begun to refract; therefore the loads will be more distributed among all legs of the buoy, reducing the load on the port line.

Table 1-9: Directional Case Simulation Results

Case	Direction [degrees]	Peak Line Load-Port [kN]	Peak Anchor Load-Port [kN]
1	0	1833	1710
2	15	2037	1960
3	30	2205	2139

1.3.2.1.2.2 Viscous Loss Study

Because of the importance of the drag coefficient in Morison's Equation, and the uncertainty of drag coefficient values in oscillatory flow, it was decided to run the severe weather mooring line analysis with multiple drag coefficients to determine the robustness of the mooring solution. The base case has the following drag coefficients, Cdx = 1.2, Cdy = 1.2, Cdz = 5, and fundamental results are summarized in Table 1-10.

Table 1-10: Base Drag Case Simulation Results

Base Drag Fundamental results (Incident Direction 30º)			
	Port	**Stbd**	**Aft**
Hangoff Max Tension [kN]	2205	1360	39
Anchor Max Tension [kN]	2139	1263	20
Chain Max Tension [kN]	2196	1335	40
Polyester Max Tension [kN]	2205	1360	41
Layback [m]	648	422	67

The maximum hangoff tension has a 1.65 factor of safety for the chain and a 2.61 factor of safety for the polyester. A lower safety factor is allowable for the chain because of its long historical use in offshore mooring systems. The anchor holding capacity of 3300 kN is sufficient and for this base drag coefficients case and provides a safety factor of 1.54.

All three drag coefficients (heave, surge, and sway) were altered on the hydrodynamic bodies of the OrcaFlex model and rerun in the same environmental condition. Peak line and anchor loads are shown in Table 1-11 for all drag run cases. Values in green are below the failure point, whereas red ones are above the mooring components breaking load.

Table 1-11: Parametric Drag Study Results

test	CD Specification			Peak Line Load-Port [kN]	Peak Anchor Load-Port [kN]
	Heave	Surge	Sway		
1	5.0	1.2	1.2	2205	2139
2	2.5	1.2	1.2	3344	3293
3	7.5	1.2	1.2	2019	1948
4	5.0	2.5	1.2	3526	3509
5	5.0	5.0	1.2	5324	5325
6	5.0	1.2	2.5	3547	3535
7	5.0	1.2	5.0	5561	5560
8	5.0	2.5	2.5	4670	4668
9	7.5	5.0	5.0	7802	7809

The only case that has a reduced load is the 7.5 heave case. All other cases see highly increased loads. Current line specifications would still be good in the double surge or sway drag coefficients cases, but there would be no safety factor.

These results highlight the importance of these hydrodynamic properties. If the assumptions used for the drag values (Cdx = 1.2, Cdy = 1.2, Cdz = 5) are shown to be incorrect through model testing it is possible that the mooring specifications could be insufficient

1.3.2.1.3 Mooring Specifications

The mooring specifications are described in Table 1-12.

Table 1-12: New Mooring System Specifications (810m Forward Line Lengths)

New Mooring System Specification										
		Port			Starboard			Aft		
Total Length	[m]	810			810			200		
Polyester length	[m]	45			45			45		
Chain length	[m]	765			765			155		
Line Length in Water Column	[m]	137.5			137.5			103.5		
Declination Angle	[deg]	122.8			122.8			113.9		
Initial Tension	[kN]	110.4			110.4			18.4		
Anchor Location	[m]	x	y	z	x	y	z	x	y	Z
		-705.4	-401.38	-59.6	-705.4	401.38	-59.6	200	0	-59.6
Attachment on OWC	[m]	x	y	z	x	y	z	x	y	Z
		-8.75	-13.25	-8.75	-8.75	13.25	-8.75	26.25	0	-8.75

The diameter and breaking load for the mooring lines are shown in Table 1-13.

Table 1-13: Mooring Lines Specifications

Lines		R4 Chain	Polyester
Diameter	**[mm]**	58	137
Diameter	**[in]**	2.28	5.5
Breaking Load	**[kN]**	3628	5754

Anchor recommendations are made using the Stevpris Mk6 anchor[24] as a reference.
For the fore anchors, a 3300 kN (335 Te) holding load is recommended. For the aft line, the smallest Stevpris Mk6 anchor is sufficient, having a holding load between 510 and 883 kN depending on the type of soil. Characteristics of the anchors are shown in Table 1-14 and Table 1-15. The soil at the test site is believed to be soft clay, but would need to be confirmed with core samples from the site.

Table 1-14: Forward Anchor Specifications

Fore Anchors:	Holding Load 3300 kN (335 Te)		
Soil Type	**Mk6 Mass (Te)**	**Drag (m)**	**Penetration (m)**
Sand/Hard clay	3.8	22	3.2
Medium Clay	5	40	7
Soft Clay	7	70	14

Table 1-15: Aft Anchor Specifications

Aft Anchor				
Soil Type	**Mk6 Mass (Te)**	**Drag (m)**	**Penetration (m)**	**Hold Load (kN)**
Sand/Hard clay	1	14	2.1	882.9
Medium Clay	1	25	4.2	706.32
Soft Clay	1	38	7.5	510.12

1.3.3 Power Conversion Chain (PCC) Design

The design of a deployable OWC device consists of two major parts: the design of the wave-to-pneumatic power converter, and the design of the pneumatic-to-electric power conversion equipment.

The wave-to-pneumatic converter is designed to capture the most available power from the incident waves. This is dictated mainly by the physical structure and the controls (implemented through the power conversion chain) used to influence the dynamics of the physical structure. The pneumatic power is then converted to electrical power by use of an air turbine connected to

an electric generator. The electricity produced is conditioned prior to insertion to the local power grid.

The BBBD performance model optimizes the pneumatic power available to the PCC. The pneumatic power is represented by the root-mean-square (RMS) pressure and volume flow rate predictions for each sea state in the wave climate. The PCC optimization then uses the sea state RMS values in combination with experimental Wells Turbine efficiency values to optimally size the turbine, generator, variable frequency drive (VFD), and downstream power electronics. The pneumatic power is then decremented by the Wells Turbine, generator, VFD, and power electronic efficiencies for each sea state. Since the RMS pressure and flow are used, this method applies only one efficiency value for the Wells Turbine in a given sea state regardless of the fact that a given sea state contains a distribution of pressure and flow values. This methodology is repeated for each sea state in the JPD assuming this single parameter representation as opposed to a full stochastic analysis as seen in Falcao et. al., 2002.[25] The average annual pneumatic (absorbed), mechanical, and electrical power (AAP, AAMP and AAEP respectively) are then calculated based on the JPD for Eureka as shown in Table 1-1.

The methodology to compute the optimal RMS flow and pressure values are detailed in the wave-to-pneumatic performance section. The pneumatic-to-electric performance section then details the components of the power conversion chain and the optimization procedure employed to determine the final PCC specifications and performance estimates for this device, as specified in the final subsection (Section 1.3.3.3).

1.3.3.1 Wave-to-Pneumatic Performance

Two conference publications detail the wave-to-pneumatic performance of the BBDB. The first was presented at EWTEC 2013[2] and it details the monochromatic performance model. The second was presented at METS 2014[7] and it details the random wave performance of the BBDB studied for RM6. More detailed explanations can be found in either of these papers. Any forthcoming papers on the BBDB reference model will be published at the RM6 publication list (www.sandia.gov/rmp/).

1.3.3.1.1 BBDB Performance Model

The offshore OWC RM6 device floats, which uniquely requires that both the wave activated body and the OWC are modeled in a coupled fashion as each absorbs power from the waves. It is the relative motion between the device and the internal free surface that produces air flow and hence power.

There are two approaches to modeling the free surface: a rigid weightless piston[26] or calculation of the pressure distribution. [27], [28]. The first approach is only valid for small internal free surface areas and is akin to a 2-body treatment in which the oscillating structure and the OWC are treated independently and will not be pursued here. The second approach does not place limitations on the size of the internal free surface area and utilizes a Boundary Element Method (BEM) solver to model the dynamics of the floating body and the fluctuating air-pressure. Calculation of the internal pressure distribution, when using a BEM solver, can be obtained in three ways: approximated, solved for explicitly, or solved for implicitly. [29], [30] Approximation utilizes the technique of generalized modes [29] which expands upon the rigid

piston approximation to include additional higher order modes. Explicit calculation requires determination of the velocity potential for the free surface. This is currently possible in WAMIT v7.0 [22], however this capability is new and uncommon in other potential flow solvers. Implicit calculation utilizes reciprocity relations to solve for all of the free surface parameters from the oscillating structure potential using an array of field points on the internal free surface. Implicit calculation, presented in [30] and [31] and applied by [20], is pursued here, allowing for the use of standard potential flow solvers such as WAMIT v6.4 [32].

The geometry of the BBDB was taken from the simplified design as presented in 1.3.1.3.

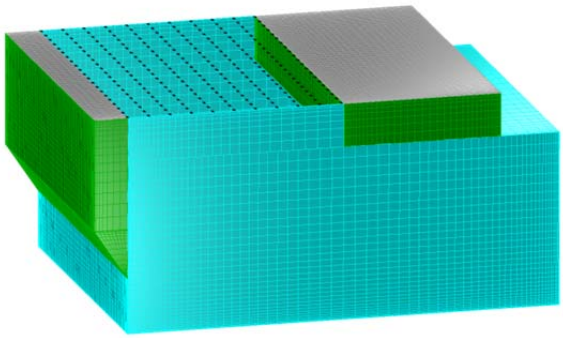

Figure 1-13: Wetted surface geometry modeled with cosine spacing in MultiSurf. Dipole panels (cyan), conventional body panels (green), interior surfaces for irregular frequency removal (gray). Black points illustrate the interior field point locations.

Panels representing the 3-dimensional wetted surface of the BBDB are used by the BEM potential flow solver. Figure 1-13 illustrates the discretization of panels as well as the types of panels used to solve for the hydrodynamic parameters. The structure panels (green) calculate the wave source potential to obtain the velocity potential. The dipole panels (cyan) obtain the velocity potential without calculation of the source potential. Meanwhile, the grey panels facilitate the removal of irregular frequencies resulting from calculation of the source potential when there is a large waterplane area. Cosine spacing is applied to the panels to increase the accuracy of the calculations close to the corners. The higher-order panel method is used in WAMIT. Only half of the device is modeled due to the device plane of symmetry at $y = 0$.

An array of 231 field points describing the interior free surface of the BBDB is defined with respect to the global coordinate system. This array is illustrated in Figure 1-13 with black points. The field points capture the dynamic pressure and velocity distributions of the free surface. Details on obtaining the hydrodynamic parameters, for both the floating body and for the free surface, can be found in the paper by Bull and Johnson.[2]

1.3.3.1.1.1 Linked Governing Equations for a Floating OWC

A linear frequency-domain model is used to produce estimates of the power conversion capabilities of the device presented in Figure 1-11. There are two governing equations: one for the oscillating structure and one for the fluctuating air-pressure. The power conversion chain links the oscillating structure to the OWC through the resistive damping term R_{load}.
The governing equation for each mode of the oscillating structure is given by:

$$i\omega m_{jj'}u_j = \left(f_j A - \left(b_{jj'} + i\omega a_{jj'}\right)u_j - \left(-H_j^u + T_j S\right)p\right) - \left(\frac{1}{i\omega}C_{jj'}u_j\right) - \left(\frac{1}{i\omega}K_j u_j\right) - \left(b_{vis,j}u_j\right) \quad (4)$$

where the left-hand side of the equation is the total force acting on the body. The first term on the right-hand side is the hydrodynamic contribution. The second term, technically part of the full hydrodynamic contribution, is the hydrostatic restoring force. The third and fourth terms are added to account for additional forces affecting the device: the mooring restoring force and the linearized viscous damping both represented here as diagonal matrices.

The hydrodynamic contribution is composed of the superposition of the:

- excitation solution found from the incident and diffracted potentials f_j multiplied by the incident wave amplitude A,
- the radiation solution found from the radiation potentials $\left(b_{jj'} + i\omega a_{jj'}\right)$ multiplied by the velocity of the body u_j in that mode (where $Z_{jj'} = b_{jj'} + i\omega a_{jj'}$ is the radiation impedance of the j^{th} mode due to unit-oscillation in one of the six j' rigid body modes),
- and a coupling term H_j^u modified by the transformation vector $T_j S$ to account for the pressure-volume flow that occurs due to the velocity of the body at the center of the free surface multiplied by the pressure p uniting them together (note the coupling term is found by evaluating the radiation vertical velocities at each field point, and hence are dependent on the rigid-body mode).

A Wells Turbine, which possesses a linear relationship between pressure and flow, is assumed in this performance model. Since air is highly compressible, accurate predictions of the air flow through the Wells Turbine require a linear representation of this compressibility. The governing equation for the relative air flow through the Wells Turbine is given by:

$$\left(\frac{1}{R_{load}} + i\frac{\omega \forall_o}{\gamma p_{atm}}\right)p = \left(qA - (G + iB)p - \sum_j \left(H_j^u + T_j S\right)u_j\right) - \frac{1}{R_{vis}}p \quad (5)$$

where the left-hand side of the equation is the total compressible relative air flow through the Wells Turbine (consistent with [33]) with no limitation on the pressure allowed within the air-chamber. The linearized air compressibility is defined through the following terms: the initial volume is $\forall_o$, $\gamma = 1.4$ and is the ratio between the constant-pressure and constant-volume specific heats for air, and p_{atm} is the atmospheric pressure. The first term on the right-hand side is the hydrodynamic contribution. The second term is added to account for the viscous damping in a linearized manner. Note that smaller R_{vis} results in greater losses of the volume flow. This inverse representation has been selected based on the formalism developed in [31] where analogs to electric circuitry are heavily employed and admittance is the inverse of impedance.

The hydrodynamic contribution is composed of the superposition of the:

- excitation volume flow q multiplied by the incident wave amplitude A,
- the radiated volume flow Y multiplied by the pressure p in the air chamber,
- and the sum of the coupling terms $H_j^u + T_j S$ multiplied by the velocity of the body u_j in that mode uniting them together.

These coupled governing equations are most readily understood in matrix notation as follows:

$$\begin{pmatrix} \boldsymbol{f} \\ q \end{pmatrix} A = \begin{pmatrix} \boldsymbol{Z}_i & -\boldsymbol{H}_i \\ \boldsymbol{H}_i^T & Y_i + \dfrac{1}{R_{load}} \end{pmatrix} \begin{pmatrix} \boldsymbol{u} \\ p \end{pmatrix} \quad 6$$

where the bolded quantities are matrices or column vectors and:

$$\boldsymbol{Z}_i = \boldsymbol{b} + \boldsymbol{b}_{vis} + i\omega \left(\boldsymbol{m} + \boldsymbol{a} - \frac{(\boldsymbol{C} + \boldsymbol{K})}{\omega^2} \right), \quad 7$$

$$\boldsymbol{H}_i = \boldsymbol{H} + \boldsymbol{T}S, \text{ and} \quad 8$$

$$Y_i = \left(G + \frac{1}{R_{vis}} \right) + i \left(B + \frac{\omega \forall_o}{\gamma p_{atm}} \right). \quad 9$$

The linked governing equations above can then be solved to obtain the linked body velocity response amplitude operator (RAO) and the linked relative pressure RAO. The RAOs are the response of a variable at a given frequency per unit incident wave amplitude A. The relative volume flow through the Wells Turbine may be derived from:

$$Q_T = qA - Y_i p - \boldsymbol{H}_i^T \boldsymbol{u} = \frac{p}{R_{load}}. \quad 10$$

From the relative volume flow, the relative interior free surface elevation may then be derived from:

$$\frac{\xi_{\text{Rel,FSE}}}{A} = -\frac{{}^{Q_T}/_A}{i\omega S}. \quad 11$$

The negative sign in Eq. 11 reflects the fact that positive volume flow into the air-chamber occurs for a decreasing free surface elevation.

The power absorbed by the coupled and linked device is dependent upon the R_{load} applied at the air turbine. The pneumatic power available to the Wells Turbine from the air-column is the product of the relative pressure in the air-chamber and the relative volume flow [31]

$$\langle P \rangle = \overline{p(t) Q_T(t)} = \frac{1}{2} Re\{p Q_T^*\}. \quad 12$$

The pressure, p, is found through solution of Eq. 12 and is the relative pressure resulting from both the movements of the structure as well as the water column. In monochromatic waves, the average pneumatic power simplifies to

$$\langle \mathrm{P} \rangle = \frac{1}{2}\frac{1}{R_{load}}|p|^2. \quad 13$$

The magnitude of the resistive damping term will impact the pneumatic power available to the Wells Turbine by influencing both the motion of the device as well as the water column. The optimal resistive damping term can then be found from the solution to the following optimization condition

$$\frac{\partial \langle \mathrm{P} \rangle}{\partial R_{load}} = 0. \quad 14$$

where $\langle P \rangle$ is the average power presented in Eq. 13. Application of the optimization condition presented in Eq. 14 results in the following analytic form of the frequency dependent optimal resistive damping:

$$R_{l_{opt}} = \left(\left|Y_i + \boldsymbol{H}_i^T \boldsymbol{Z}_i^{-1} \boldsymbol{H}_i\right|^2\right)^{-\frac{1}{2}}. \quad 15$$

Eq. 15 is the optimal resistive damping for a floating OWC first presented in [2]. If the structure were fixed, the optimal R_{load} would consist of only the first term in Eq. 15. However, since the structure is floating, and also absorbing power from the incident waves, the optimal resistive damping must reflect the contribution from the floating structure. Hence the additional term relating to the magnitude of coupling $\boldsymbol{H}_i$ and the radiation impedance $\boldsymbol{Z}_i$ of the structure in the analytic form of the optimal R_{load} is reasonable. Inserting Eq. 15 into Eq. 13 produces the maximum pneumatic power in monochromatic waves.

1.3.3.1.1.2 Hydrodynamic Coupling between the Structure and the Water Column

The effect of hydrodynamically coupling the structures motions to the water column is the migration of the water column natural resonance frequency, even when the air chamber is fully vented to atmosphere. The total hydrodynamic flow and its resonance frequency are influenced by both the magnitude of the coupling term (driven by the total surface area) and the number of rigid body modes through which coupling occurs. Figure 1-14 shows the volume flow RAO for a fully vented air chamber (i.e. the device is not linked with a control strategy). The floating BBDB device is compared to its hydrodynamically uncoupled counterpart. The hydrodynamically uncoupled counterpart is physically the grounded version of the device, i.e., there is no wave-activated body motion. It is clear from Figure 1-14 that natural resonance of the water column for the floating device is very distinct from the one predicted for a grounded device.

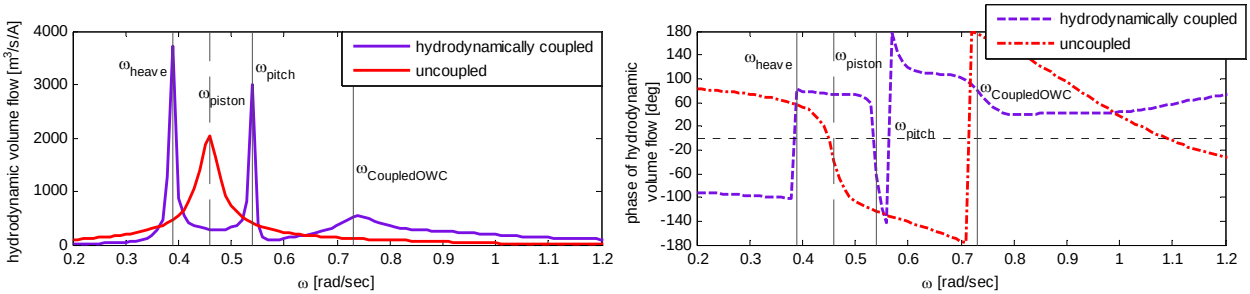

Figure 1-14. Confirmation of the migration of the water column natural resonance due to hydrodynamic coupling for the BBDB.

This natural resonance migration had not been previously reported in literature. Hence experimental verification of this new result was pursued in this program; more detail on the experimental campaign can be found in the report by Bull, Gunawan and Holmes.[8] The experiments were conducted at HMRC at University College Cork in Ireland. The device was tested using Froude scaling with a scaling factor of 50. The device motions and the internal free surface elevation (FSE) were tracked in three dimensions with a Qualisys system. The port and starboard sides of the free surface were measured. A pressure sensor recorded the pressure inside of the air chamber.

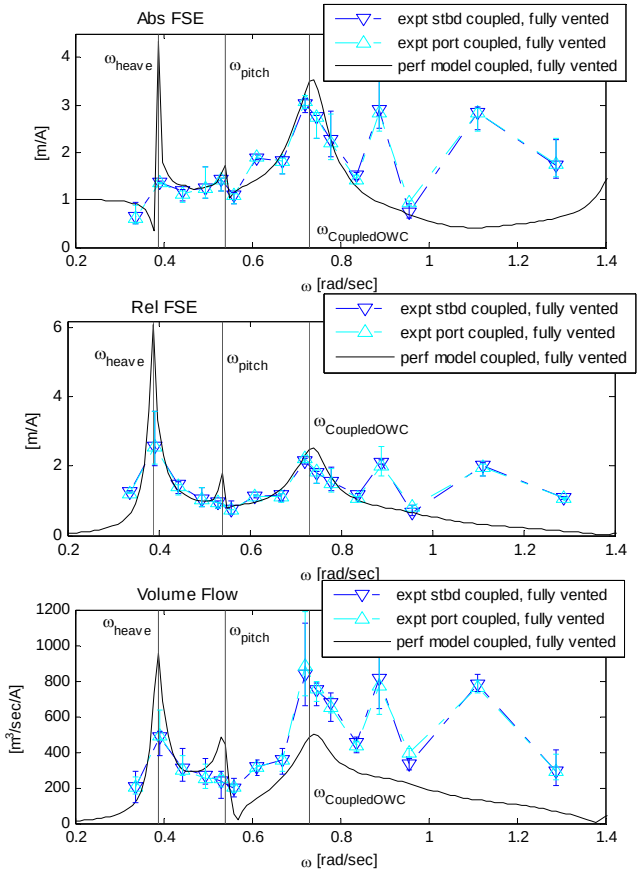

Figure 1-15: Experimental verification of $\omega_{copuledOWC}$ through RAOs of absolute FSE, relative FSE, and volume flow for a fully vented BBDB.

Figure 1-15 compares the experimentally determined RAOs with the predicted results (at full scale) for a fully vented air chamber. The FSE plots (both absolute and relative to the structure) confirm the predicted hydrodynamically coupled OWC resonance frequency by exhibiting a large response from both the port and starboard measurements at that frequency. Further, the experimental volume flow RAO confirms the predicted shape. There is no evidence of $\omega_{piston} = 0.46$ in the experimental data.

As shown above, the experimental results confirmed the underlying physics of the performance model presented in Eq. 15. Again, more detail on the experimental campaign can be found in the 2014 SAND report.[8]

1.3.3.1.1.3 Performance Results Monochromatic Waves

Viscous damping terms were selected in order to reduce the magnitudes of the linked body motions and free surfaces elevations at resonance. Constant (and diagonal when applicable) damping values for both the body and the free surface are applied across all frequencies. For the presented solutions these are: $b_{vis} = 0.02 * 2\sqrt{M_{tot}c_{tot}}$ and $R_{vis}^{-1} = 0.01(\max(G))$. M_{tot} is the physical mass in combination with the infinite frequency added mass and c_{tot} is the total restoring force (hydrostatic plus mooring). The magnitude of these additional viscous damping terms should be verified with experimental tests. However the presented values are able to reduce RAO magnitudes to reasonable levels.

The mooring restoring force is obtained from the mooring design detailed in [5]. The design was found to act linearly for excursions of $\pm$5m in the surge, sway, and heave directions. The magnitudes of the restoring forces are: 55.5 kN in surge, 6.1 kN in sway, and 7.5 kN in heave.

Figure 1-16 compares the analytic expression of $R_{l_{opt}}$ from Eq. 15 as a function of frequency to a numeric optimization. The difference between the curves is solely a result of the fidelity of the numeric optimization, which confirms the solution presented in Eq. 15. Since both the body motions and the free surface are accounted for in the relative pressure term, the profile of $R_{l_{opt}}$ experiences multiple distinct minima corresponding to natural resonances for the coupled device. The structural resonance locations and the coupled OWC resonance location are identified in Figure 1-17 for clarity (solid and dashed vertical lines, respectively). Between these minima, $R_{l_{opt}}$ increases resulting in three resistive damping peaks.

Figure 1-17 compares the linked and unlinked RAO's for heave, pitch, and the absolute free surface elevation (FSE) when $R_{l_{opt}}$ is applied at each frequency. The linked RAO's exhibit the unlinked natural resonances as would be expected since $R_{l_{opt}}$ is minimal at these locations. However, the linked RAO's also exhibit additional peaks that correspond to the peaks seen in$R_{l_{opt}}$.

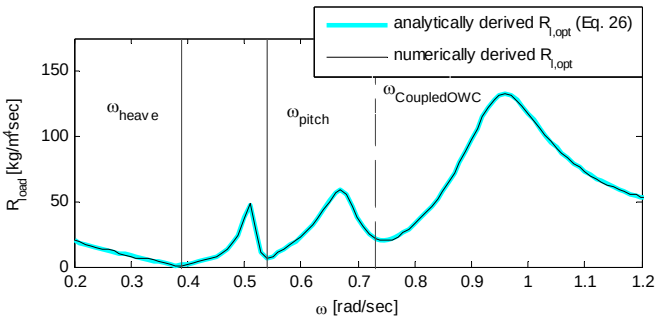

Figure 1-16: Comparison of analytically derived and numerically obtained optimal resistive damping $R_{l_{opt}}$ for a floating OWC.

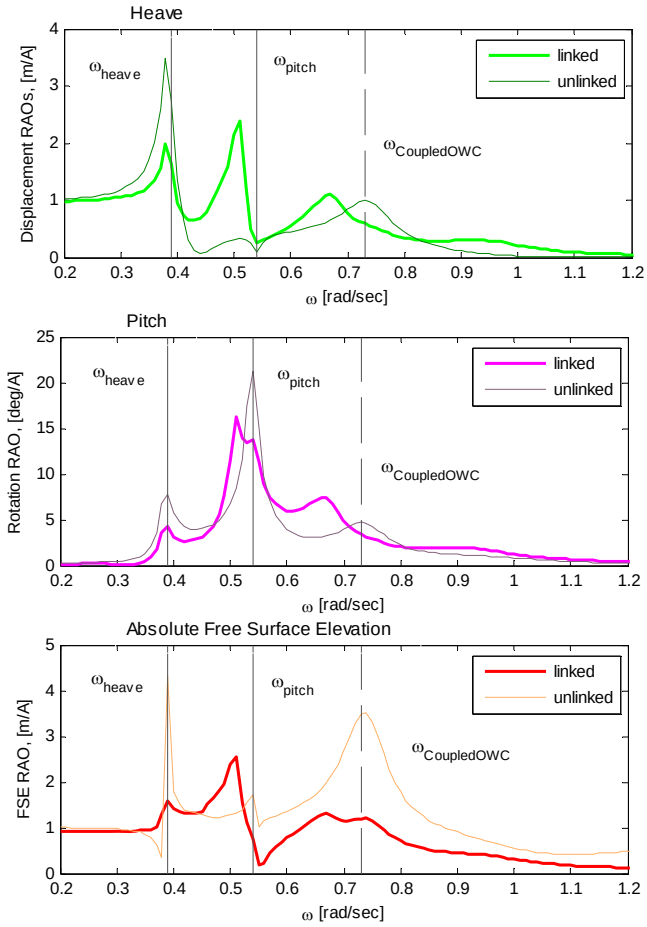

Figure 1-17: RAO's for heave, pitch, and the absolute free surface elevation when a Wells Turbine with $R_{l_{opt}}$ is applied in the linked case and when there is no Wells Turbine in the unlinked case.

The relative linked pressure is shown in Figure 1-18. The peaks in pressure correspond to the locations of increased resistive damping. Alternatively the peaks in relative volume flow, shown in Figure 1-19, correspond to resonances in the system. This inverse partnership between pressure and flow is expected: when the device is in resonance there will be large volume flow,

otherwise $R_{l_{oad}}$ will be used to increase the pressure in the air-chamber when the phase relationships have a close phase match.

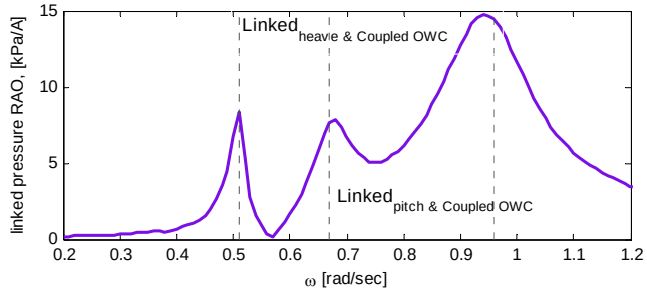

Figure 1-18: RAO of relative linked pressure with $R_{l_{opt}}$ applied.

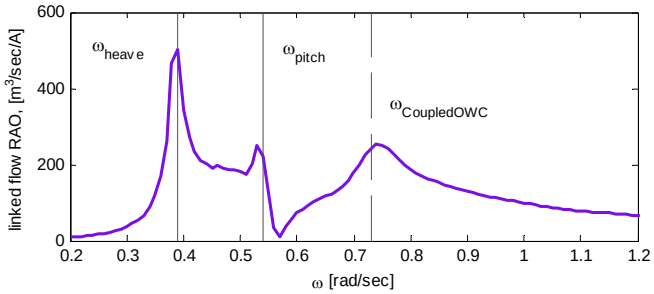

Figure 1-19: RAO of relative linked flow with $R_{l_{opt}}$ applied.

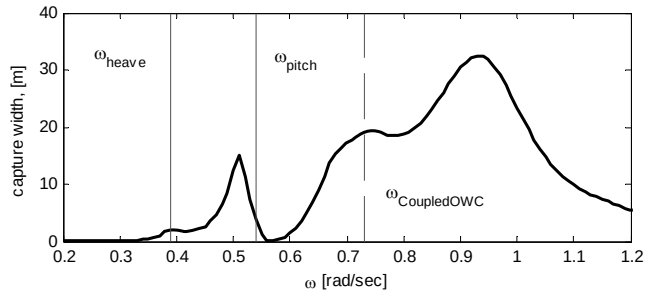

Figure 1-20: Capture width for a floating OWC with $R_{l_{opt}}$ applied at each frequency.

Finally the capture width of this device, with $R_{l_{opt}}$ applied at each frequency, is shown in Figure 1-20; the locations of the resonances are identified. Both the heave and the coupled OWC resonance contribute to the capture width. The pitch natural resonance is not detectable, but it is likely that it has been subsumed into the linked heave-coupled OWC peak. The three peaks in Figure 1-16 that result from the phase matching between degrees of freedom strongly affects the structure of the capture width. Linking the structure to the OWC through the Wells Turbine and applying $R_{l_{opt}}$ results in the largest power conversion at these linked peaks.

Although coupling between the structure and the OWC is often mentioned as a benefit of the BBDB design, this is the first presentation to the authors' knowledge that demonstrates the linked heave-coupled OWC and linked pitch-coupled OWC modes. These linked modes expand the area of power conversion and cannot be ignored.

1.3.3.1.2 BBDB Performance in Random Waves

The monochromatic BBBD performance model must be expanded to understand how the device will respond to random waves. Since the response of the device is linear, the spectral response of the device will follow the spectrum describing the incident climate.

In order to transform from monochromatic to spectral response, relevant RAOs and the wave spectrum S(ω) that the device will be subject to are required. The variables' RAO will not apply $R_{l_{opt}}$ as specified in Eq. 15. The optimal R_{load} for each sea state is thus found through numeric optimization. This procedure assumes that only one R_{load} can be applied for the duration of the sea state and hence one R_{load} is applied across all frequencies.

In this case, the devices response in each sea state was obtained for R_{load} spanning 1-200 Pa/m^3/sec in increments of 1 Pa/m^3/sec. The optimal value is the one that produces the largest average power in the sea state (as described below in Eq.16). There are more advanced algorithms that will more accurately identify the true maximum power (see [34] for example), however they were not utilized in this study. Figure 1-21 shows the results of the optimization.

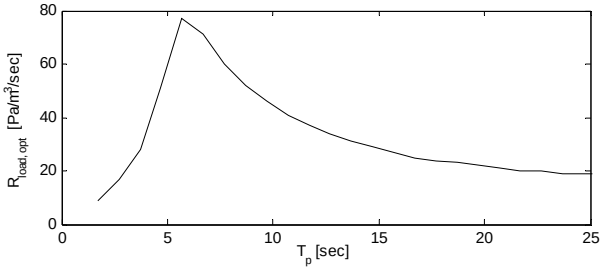

Figure 1-21: Optimal R_{load} for Tp

The response spectrum, S_R, for any variable R can then be obtained through the following calculation:[35]

$$S_R(\omega) = RAO(\omega)^2 S(\omega) \quad (16)$$

The RAO has units of response per unit wave amplitude (i.e. Pa/m, N/m, etc.), the wave spectrum has units of (height)^2-time (i.e. m^2-s), and hence the response spectrum will have units of (response unit)^2-time (i.e. Pa^2-s, N^2-s, etc.). Figure 1-22 below illustrates the required inputs and the resulting spectral density for the volume flow in the BBDB.

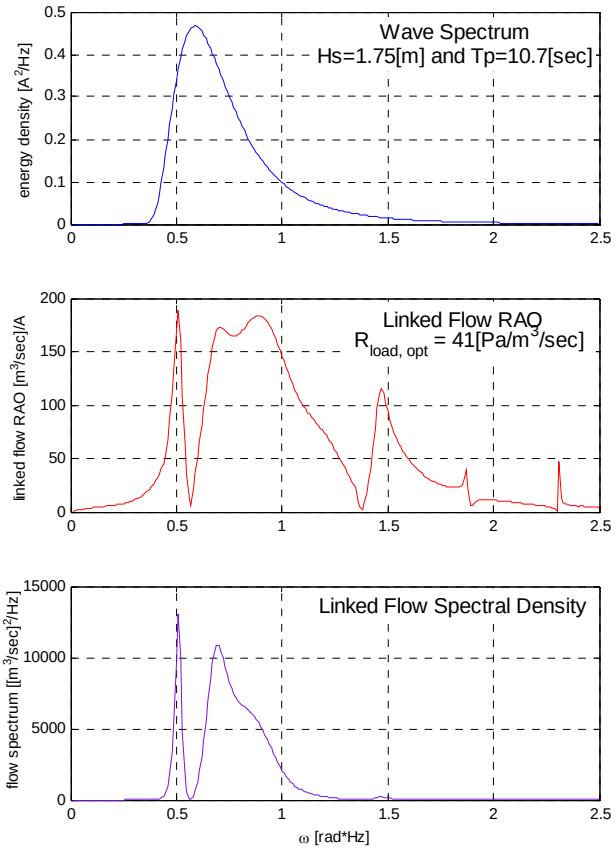

Figure 1-22: Flow Spectral Density Calculation

Relevant statistical parameters can be calculated from the variable's spectral density since the structural response will also be stationary and random, following a Gaussian distribution. The root-mean-square (RMS) and significant values, as shown in Eq.'s 17 and 18 respectively, can be calculated for any variable R.

$$R_{RMS} = \sqrt{\int S_R(\omega)d\omega} = \sqrt{m_0} \quad 17$$

$$R_s = 2\sqrt{\int S_R(\omega)d\omega} = 2\sqrt{m_0} \quad 18$$

Above, m_0 is the zeroth moment of the spectral density. The integrals in Eq. 17 and 18 are approximated using trapezoidal summation over the frequency range defined by the WAMIT run.

The average absorbed power in the sea state is calculated using the spectral density calculation for either the flow or the pressure in the air chamber. Eq. 19 below shows the calculation using flow.

$$\langle P_{ij} \rangle = R_{load,i} \int \mathrm{Q}_{T,ij}(\omega)^2 S_{ij}(\omega)d\omega \quad 19$$

Alternatively, the average power can be obtained through the product of the RMS pressure and flow, as derived from the spectral density. This absorbed power is often referred to as the pneumatic power for OWC devices.

Since the device is modeled linearly in the frequency domain, increasing H_s for a particular T_p multiplicatively increases $\langle P \rangle$. Hence, the capture width is often used to represent the response of a device to incoming seas. This measure of efficiency is obtained through a ratio of absorbed power in a particular sea state to the incident wave power in that sea state:

$$\chi_{w,i} = \frac{\langle P_i \rangle}{J_i}. \qquad 20$$

The spectral capture width is a function of T_p and when compared to ζ_{T_p} allows the device designer to quickly assess the compatibility between device performance and energy weighted deployment climate characteristics. Figure 1-23 illustrates this comparison.

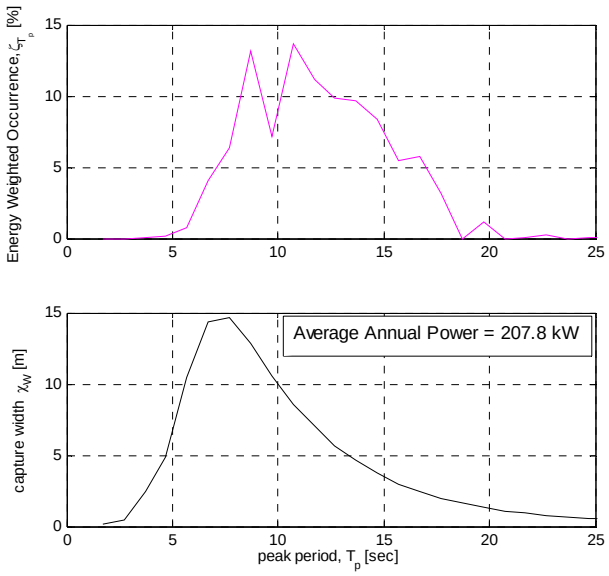

Figure 1-23: Energy Weighted Occurrence and Spectral Capture Width of BBDB

Comparison of the spectral capture width χ_w with ζ_{T_p} shows that the device may be designed more effectively for this control strategy by instituting changes that would shift the peak of χ_w towards longer periods. This finding is interesting since the natural periods indicated in Figure 1-17, Figure 1-18, Figure 1-19, Figure 1-20 and Figure 1-21 align so well with ζ_{T_p}. This is likely due to the control strategy implemented in this model: a constant R_{load} for all frequencies in a sea state.

1.3.3.1.3 Performance Model Remarks

An experimentally verified performance model was used to produce estimates of the performance of the BBDB in a Northern California deployment climate. However, there are a few key modeling choices that contribute to the uncertainty of the attainable average annual power magnitude. These choices include:

- Using a linear frequency domain model,
- Using uni-directional and perpendicular incident irregular wave sea-states,
- Selecting viscous loss values that were not calibrated experimentally,
- And, employing a simple resistive control strategy that required a linear relationship between flow and pressure.

A more advanced performance model capable of producing more accurate results would address most, if not all, of the issues identified above.

1.3.3.2 Pneumatic-to-Electric Performance

Two publications detail the power conversion chain design of the BBDB. The first was presented at METS 2104[9] and it highlights some of the optimization work that was completed to determine the PCC. The second is a SAND report[36] more fully detailing the optimization procedure used to determine the final configuration of the PCC.

1.3.3.2.1 Mechanical Conversion: the Wells Turbine

The Wells air turbine is a power extraction device capable of collecting power in a bi-directional flow. It is attractive for use in OWC devices owing to the bi-directional nature of the flow in such devices. The Wells turbine consists of a fixed number of blades, which typically have a symmetric airfoil profile, and which have the blade chord oriented perpendicular to the rotational axis of the rotor. See Figure 1-1.

Although there are many turbine types that could have been considered to produce mechanical power, this reference model only considered the Wells Turbine due to its linear characteristics. Only a linear frequency-domain model was available to predict the absorbed (pneumatic) power and hence a turbine with linear characteristics had to be modeled regardless of their relatively low efficiencies in comparison to other choices.

For a single RPM and tip diameter the relationship between the non-dimensional flow rate coefficient, ϕ, and the non-dimensional pressure coefficient, ψ, is approximately linear for the Wells Turbine. This is verified in Figure 1-24 from Starzmann et al. 2012.[37] The non-linear portion of Figure 1-24 is caused by aerodynamic stalling due to large flow incidence angles and the effects of compressibility on the rotor blades.

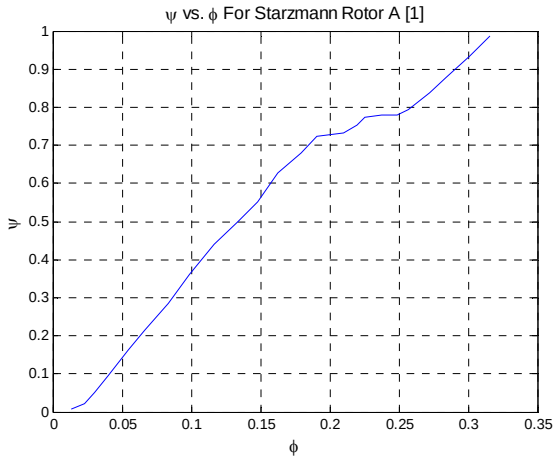

Figure 1-24: ψ vs. φ for Starzmann rotor a [1], typical for other turbine designs used in the current studies.

The performance of the Wells turbine depends on the specific design of the turbine blades and any other features, such as variable pitch blades or the use of guide vanes. Performance data is typically collected on small scale versions of the Wells turbine and is reported as the non-dimensional pressure head coefficient ψ and the turbine efficiency η versus the non-dimensional flow coefficient ϕ. The efficiency versus flow coefficient curves for the various turbine designs used in the present studies are shown in Figure 1-25[37]–[39] where ϕ is defined by Equation 21.

$$\phi = \frac{U}{\omega R} = \frac{Q_T}{\frac{\pi^2}{4} D^3 n} \qquad 21$$

Where U is mean axial velocity, ω is the turbine rotational speed in rad/s, R is the turbine tip radius, Q_T is the volumetric flow rate through the turbine, D is the turbine tip diameter, and n is the turbine rotational speed in rev/s. Notice that peak efficiency for fixed pitch type turbines is larger than for variable pitch type turbines. However, peak efficiency comes at the cost of efficiency bandwidth across the non-dimensional flow coefficient,ϕ. Varying the turbine pitch allows the turbine to adapt to a wide range of flow coefficients, which accounts for the increased efficiency bandwidth. The shift in the efficiency curve for the variable pitch turbine is a result of the test turbine in Gato et. al. acting as a fan for lower flow coefficients.[39]

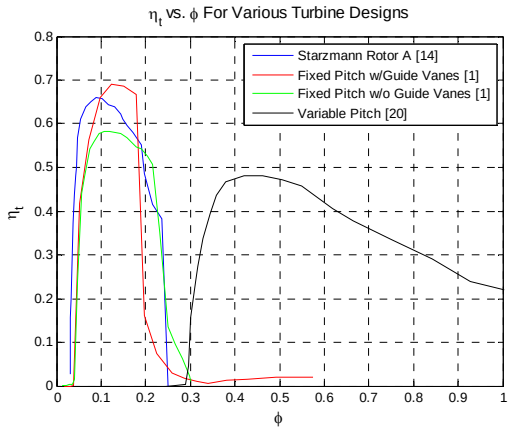

Figure 1-25: Wells turbine efficiency vs. flow coefficient for various turbine designs.

Brito-Melo, et. al.[38] suggest that the use of a pressure relief valve for flow control is able to maintain flow coefficients near the point of peak efficiency. Another method for maintaining flow coefficients near the peak efficiency value is by variation of the turbine rotational speed.

1.3.3.2.2 Electrical Conversion: The Generator and VFD

Using the BBDB RMS internal pressure and the optimal R_{load} shown in Figure 1-21, the volumetric flow rate through the turbine can be found according to Eq.22, where p is the RMS dimensional chamber pressure and ρ is the density of air at sea level conditions.

$$R_{load} = \frac{p}{Q_T} = \frac{\psi}{\phi}\frac{n\rho}{R} \qquad 22$$

In order to achieve varying R_{load} values for a fixed turbine radius the rotational speed of the turbine must vary. It is assumed that rotational speed is a constant for each individual sea state, that rotational speed changes between sea states, and oscillations in rotational speed as a result of inertial storage in the Wells Turbine are small. Varying the turbine RPM will change the non-dimensional flow coefficient in the turbine, which could result in operating at non-peak turbine efficiencies. The turbine RPM required to achieve the optimum R_{load} is found using Eq. 23.

$$n = \frac{\phi}{\psi}\frac{R}{\rho}R_{load} \qquad 23$$

The VFD is a crucial component for the control of the OWC system and for generation of electricity at variable speeds. There are several types of VFDs available on the market today. The VFD selected is a four quadrant VFD. This means that the VFD can accept electric power from the grid and transform the voltage and frequency of the electricity to the appropriate values in order to spin the turbine up to a certain speed. Then when the turbine begins to be driven by the flow the VFD has an additional inverter built in, which gives it the capability to transform the electric power being produced by the turbine and generator (which is being produced at a

variable frequency) into power conditioned for depositing to the grid (480 V, 60 Hz). A control system can be implemented which can control the turbine rational speed based on the sea state or the flow rate through the system. The control system design would be a part of the detailed design of the four quadrant VFD.

With the RPM calculated and turbine radius known the non-dimensional flow coefficient can be determined according to Eq.21. This is then used to look up turbine efficiency, η_t, based on small scale test data from Figure 1-25.

Usage of efficiency data from these small scale experiments neglects the effects of Reynolds and Mach numbers. With η_t known, the mechanical power, M_{ij}, available to the electricity generation equipment for each sea state is found using Eq.24.

$$M_{ij} = p_{RMS_{ij}} Q_{T,RMS_{ij}} \eta_t . \qquad 24$$

The total efficiency of the electricity generation equipment is $\eta_{elec} = \eta_{gen}\eta_{VFD}$. Once the turbine mechanical power is known, η_{gen} and η_{VFD} are found from typical generator and VFD efficiency curves[40], [41] which then allows the calculation of η_{elec}. Figure 1-26 shows an η_{elec} curve if the VFD and generator have the same power rating. Once η_{elec} is known the electric power, W_{ij}, generated by the system in each sea state is then found using Eq.25.

$$W_{ij} = M_{ij}\eta_{elec} \qquad 25$$

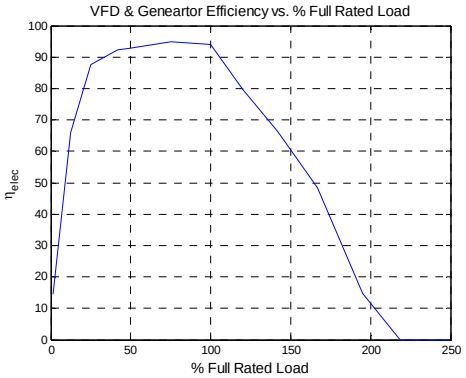

Figure 1-26: Combined VFD and Generator efficiency vs. % Full rated load of electricity generation equipment.

1.3.3.2.3 PCC Optimization Procedure

A number of design studies were conducted which attempted to locate the optimum PCC design for the provided BBDB design. These studies included variation of the turbine type, the vent pressure, the turbine radius, the number of turbines, and the power ratings of the VFD and generator. Below, these design studies will be described and their results discussed. In addition,

a global optimization study was performed and took advantage of MATLAB's Global Optimization Toolbox to vary all of the design variables at once.

The methodology followed for determining the optimum turbine tip radius, vent pressure, VFD power rating and electric generator power rating in the design studies is as follows:

1. Select a turbine type from the types indicated in Figure 1-25.
2. Specify a single tip radius, vent pressure, VFD power rating and electric generator rating.
3. Based on the required R_{load} for each sea state, calculate the rotational speed of the Wells Turbine for each sea state.
4. Calculate the flow coefficient for each sea state.
5. Find η_t and calculate mechanical power, M, for each sea state.
6. Use M and the power ratings of the VFD and the generator to determine η_{elec}.
7. Calculate the electric power, W, generated for each sea state.
8. Determine the AAEP for the turbine design, and electricity generation equipment combination.
9. Loop through all desired tip radii, vent pressures, VFD power ratings, and electric generator ratings.
10. Plot and analyze results to determine design with largest AAEP.

This methodology has been implemented using MATLAB for the following optimization studies.

1.3.3.2.3.1 Mechanical Power: Turbine Type Study

Figure 1-25 shows η versus ϕ for four different types of Wells turbines. Starzmann's Rotor A is a fixed pitch rotor, using a NACA 0021 profile at the blade base, a NACA 0018 profile at the blade midspan, a NACA 0015 profile at the blade tip, and with varying chord length along the blade span. The other types of turbines use a rotor design similar to that used by the PICO plant at the Azores, Portugal and include a fixed pitch rotor with guide vanes, the same fixed pitch rotor without guide vanes, and a variable pitch rotor .[37]–[39]

Table 1-16 shows AAEP and Significant Average Annual Electric Power (SAEP) predictions, optimum, turbine tip radius, and optimum vent pressure for the four different types of turbine using a VFD Power rating of 373 kW and a generator power rating of 298 kW. Starzmann's Rotor A achieves the largest AAEP of the four types, owing to the relatively high, and broad (relative to the other fixed pitch turbines), efficiency curve. Thus the remainder of the studies will use the Starzmann Rotor A, and will focus on the effects of the other design variables.

Table 1-16: AAEP, SAEP, optimum turbine tip radius, and vent pressure for different types of Wells turbines.

Turbine Type	AAEP (kW)	SAEP (kW)	Optimum Turbine Tip Radius (m)	Vent Pressure (Pa)
Starzmann A	103.3	229.3	1.588	5380
Fixed Pitch	74.1	182.2	0.923	6205
Fixed Pitch w/Vanes	71.6	172.1	0.987	5875
Variable Pitch	54.7	152.8	1.018	7525

The variable pitch turbine does not perform as well as the fixed pitch turbines. This is due to the use of a pressure relief valve for flow control and the treatment of the turbine efficiency as a single value for each sea state, as opposed to spectrally.

1.3.3.2.3.2 Electrical Power: Effects of VFD and Generator Rating

Table 1-16 outlines the effects of varying the VFD and generator power rating using Starzmann's Rotor A.[37] It is important to note that while a generator can maintain high efficiency values when overloaded, the VFD can only output power up to its power rating. As a result any excess power put into the VFD is dumped out of the system, causing a steep decline in efficiency when the VFD is overloaded.

From the results in Table 1-17 AAEP is maximized for a VFD/generator power rating ratio of 1.25 for the wave climate and BBDB used in these studies. Further increases of the VFD/generator power rating ratio over-rates the electricity generation equipment causing losses in efficiency, see Figure 1-26. Under-rating of the VFD or generator also causes the same, or greater, losses. Increasing the VFD or generator rating also allows for an increase in the vent pressure and an increase in turbine tip radius, up to the VFD generator rating ratio of approximately 1.25. Larger vent pressures and tip radii can lead to increases in AAEP if the flow coefficients through the turbine remain near peak efficiency.

Table 1-17: AAEP predictions for various generator and VFD power ratings.

Annual Average Power (kW)					
Generator Rating (kW) / VFD Rating (kW)	75	149	224	298	373
75	52.7	54.5	53.9	52.8	51.8
149	63.7	82.9	83.3	82.5	81.4
224	62.7	91.7	96.6	96.3	95.5
298	61.9	91.9	101.3	101.7	101.0
373	60.8	90.9	101.6	103.3	102.7
447	59.1	89.8	100.6	103.0	102.7
522	57.5	88.8	99.6	102.3	102.2
597	55.7	87.9	98.7	101.3	101.3
671	54.2	86.6	97.5	100.1	100.2
746	53.0	85.4	96.3	99.0	99.0

Figure 1-27 shows that as the generator rating increases toward a VFD Rating/Generator Rating ratio of 1.25 the losses incurred by under rating the electricity generation equipment are reduced.

At higher VFD/generator rating ratios large AAEP losses occur at lower vent pressures because the energy captured by the BBDB overloads the generator enough to cause efficiency decrements. Once the VFD/generator rating ratio reaches approximately 1.25 the AAEP ceases to be a function of the vent pressure. As a result the optimum vent pressure is selected to be at the maximum SAEP, if the VFD/generator power rating ratio is greater than 1.25. Figure 1-27 also shows that the optimum vent pressure (and subsequently the turbine tip radius and the AAEP) is limited by the power rating of the generator.

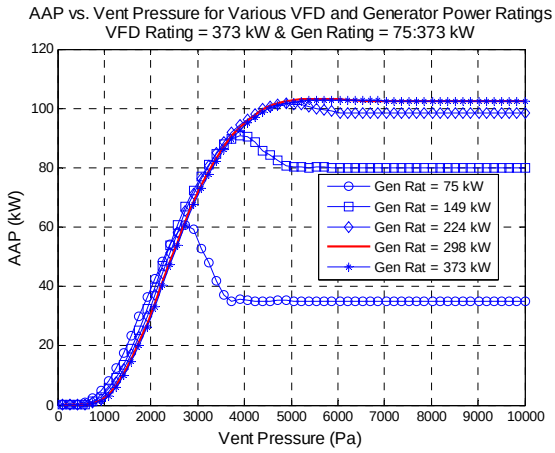

Figure 1-27: AAEP vs vent pressure for a range of generator power ratings at a VFD power rating of 373 kw.

1.3.3.2.4 Optimal Power Conversion Chain Specification

By following the procedure outlined in [9] and summarized above, the final design uses Starzmann's Rotor A at a tip radius of 1.588 m, a vent pressure of 5380 Pa, a VFD power rating of 373 kW, and a generator rating of 298 kW. A full methodology for the selection of the optimal turbine type, turbine tip radius, vent pressure, and power electronics based on the average annual performance for the entire wave climate at a specific location is presented in [36]. The predicted AAEP for this design is discussed in the section 1.3.3.3 below.

Design studies using the PCC optimization procedure are based on the devices performance in the entire wave climate. The power generation equipment consists of a Wells turbine, an electric generator, and a Variable Frequency Drive (VFD). These studies have shown:

- The largest Average Annual Power (AAEP) prediction comes from using the Rotor A design of Starzmann.[37]
- There exists an optimum turbine tip radius and vent pressure combination which will produce the largest AAEP, for a given VFD and generator combination.
- The AAEP, turbine tip radius, and vent pressure are all dependent upon the power ratings of the VFD and generator.
- Both the VFD and generator must be appropriately sized to achieve the maximum AAEP. The optimum ratio of VFD power rating/generator power rating is approximately 1.25.

- The PCC should be designed for the most energy dense sea states, instead of the most probable, in order to maximize AAEP.

The interplay between turbine size, vent pressure, VFD power rating and generator power rating is complex. These presented AAEP predictions highlight some aspects of these relationships and that without consideration of each component in the entire system the PCC design could incur large power losses.

1.3.3.2.5 PCC Design Remarks

The current work does not attempt to address the effects of Reynolds number or Mach number on the rotor blades; this nonlinearity will have a detrimental effect if the design does not put rotational speed limitations on the turbine.[42] As a result, the AAMP and AAEP predictions presented in later sections are considered ideal. Future work should include effects of compressibility on the turbine performance in the BBDB stochastic model.

The optimization procedures, both for the R_{load} as well as for the PCC components, could be improved. A fully stochastic model that accounted for the distribution of flow coefficients, and hence a distribution of mechanical conversion efficiency values, within a sea state would result in a more accurate, and likely lower, electrical power estimate.

Since this performance model is limited to linear systems, the only primary converter considered in this report is the self-rectifying Wells Turbine which possesses a linear relationship between pressure and flow. This turbine choice is no longer predominant in industry since the peak value and bandwidth of the efficiency is known to be inferior to other turbines.[43]

1.3.3.3 PCC Specifications and AAEP Estimation

The final design as discussed in 1.3.3.2.4 uses Starzmann's Rotor A at a tip radius of 1.588 m, a vent pressure of 5380 Pa, a VFD power rating of 373 kW, and a generator rating of 298 kW (the design of Figure 1-11). The predicted AAEP for this design is 103.2 kW. Hence the optimal PCC design for this device results in a rating of 373 kW with a capacity factor of 27.6.

Table 1-18 shows that 44.7% of the power losses in the PCC occur in the pneumatic-to-mechanical power conversion, while only 10.3% of the losses in the PCC are due to the mechanical-to-electrical power conversion. By selecting a more efficient turbine, the electric output of this device could be increased significantly.

An analysis as in Table 1-18 of the BBDB performance can compare the Pneumatic Power, Mechanical Power and Electrical Power produced annually. Long-term performance estimates for a device are obtained by combing results from the spectral treatments with the JPD for the deployment site. For instance the average annual pneumatic power (AAP) for the device can be obtained according to Eq. 26.

$$\mathrm{AAP} = \sum_{ij} JPD_{ij} \langle P_{ij} \rangle \qquad 26$$

Here, the power weighted matrix is obtained by multiplying the average power produced in each sea state by the probability of that sea state occurring. The sum of the power weighted matrix results in the average annual power production at the deployment location. This procedure can

be followed to obtain annual estimates of any variable: annual significant flow, annual RMS pressure, annual RMS pitch angle, etc.

Table 1-18: Annual Power for the final selected design highlighting decrement in power at each conversion step.

	AAP (kW)	% Decrease	SAP (kW)
Pneumatic Power	208	N/A	831
Mechanical Power	115	44.7	261
Electrical Power	103	10.3	229

Peak Period, Tp [sec]

Significant Wave Height, Hs [m]	4.7	5.7	6.7	7.7	8.7	9.7	10.7	11.7	12.7	13.7	14.7	15.7	16.7	17.7	18.7
0.25	1	2	3	3	3	3	3	2	2	2	2	1	1	1	1
0.75	5	14	23	28	28	27	24	22	20	17	15	13	11	9	8
1.25	14	39	64	77	**78**	74	68	61	55	48	41	35	30	25	21
1.75	28	76	125	150	153	144	133	120	107	93	80	69	58	49	42
2.25	46	126	207	249	253	239	219	199	177	154	133	113	96	82	69
2.75	69	188	309	371	378	356	328	297	264	231	199	170	144	122	103
3.25	96	262	431	519	528	498	458	414	369	322	277	237	201	170	144
3.75	128	349	574	691	703	663	609	552	491	429	369	315	268	227	192
4.25	164	448	737	887	903	851	783	709	630	551	474	405	344	291	247
4.75	205	560	921	1108	1128	1063	978	885	787	688	593	506	429	364	309
5.25	251	684	1125	1354	1378	1299	1194	1082	962	840	724	618	525	445	377
	4.0	**4.9**	**5.7**	**6.6**	**7.5**	**8.3**	**9.2**	**10.0**	**10.9**	**11.7**	**12.6**	**13.5**	**14.3**	**15.2**	**16.0**

Energy Period, Te [sec] $2\pi(m_{-1}/m_0)$

Figure 1-28: BBDB pneumatic power matrix, values displayed in kW. R_{load} as shown in Figure 1-21 applied for each peak period. Shading from scatter diagram maintained to highlight that this device performs best in waves that are not probable.

Figure 1-28 shows the average pneumatic power (in kW) produced in each sea state by the BBDB. Shading from the scatter diagram indicating wave probability is maintained to highlight that this device does not perform the best in the most probable sea states, instead it performs the best in the most energy dense sea states. These pneumatic power values were obtained by applying the R_{load} values shown in Figure 1-21.

		Peak Period, Tp [sec]														
		4.7	**5.7**	**6.7**	**7.7**	**8.7**	**9.7**	**10.7**	**11.7**	**12.7**	**13.7**	**14.7**	**15.7**	**16.7**	**17.7**	**18.7**
Significant Wave Height, Hs [m]	**0.25**	0	0	0	0	0	0	0	0	0	0	0	0	0	0	0
	0.75	0	0	0	0	1	1	1	1	1	3	3	3	3	3	2
	1.25	0	0	1	2	**13**	27	32	35	32	29	25	22	19	16	13
	1.75	1	1	3	49	81	87	83	77	69	61	52	45	38	32	27
	2.25	1	3	41	139	157	153	143	130	116	101	87	74	63	53	45
	2.75	8	5	132	229	244	233	216	194	171	148	127	109	92	78	66
	3.25	33	51	225	308	346	327	297	266	235	201	171	144	121	103	88
	3.75	60	131	225	308	366	409	390	344	297	253	216	182	152	130	112
	4.25	95	153	225	308	366	409	444	419	365	304	248	199	160	140	123
	4.75	124	153	225	308	366	409	444	456	399	309	256	209	172	149	128
	5.25	156	153	225	308	366	409	444	456	402	332	279	193	104	120	126
		4.0	**4.9**	**5.7**	**6.6**	**7.5**	**8.3**	**9.2**	**10.0**	**10.9**	**11.7**	**12.6**	**13.5**	**14.3**	**15.2**	**16.0**

Energy Period, Te [sec] $2\pi(m_{-1}/m_0)$

Figure 1-29: BBDB mechanical power matrix, values displayed in kW. Wells Turbine radius 1.588m and a vent pressure of 5380 Pa. Shading from scatter diagram maintained to highlight that this device performs best in waves that are not probable.

Figure 1-29 shows the pneumatic to mechanical power for a vent pressure of 5380 Pa, and a turbine tip radius of 1.588 m. Mechanical power becomes constant as significant wave height increases owing to the vent pressure limiting power captured by the BBDB. Also, at large wave heights and long wave periods the mechanical power drops to zero. In this region, the turbine flow coefficients are too large and cause the turbine efficiency to be zero.

In Figure 1-29 the larger vent pressure allows for more energy to be captured by the BBDB. This combined with a VFD/generator power rating ratio of 1.25 results in more efficient conversion of pneumatic power to mechanical power to electrical power. Comparison of Figure 1-28 and Figure 1-29 corroborates the analysis of Figure 1-27; the VFD and generator power ratings limit the vent pressure and turbine tip radius. These limitations reduce the amount of power that can be efficiently converted from pneumatic power to mechanical power to electrical power.

		Peak Period, Tp [sec]														
		4.7	**5.7**	**6.7**	**7.7**	**8.7**	**9.7**	**10.7**	**11.7**	**12.7**	**13.7**	**14.7**	**15.7**	**16.7**	**17.7**	**18.7**
Significant Wave Height, Hs [m]	**0.25**	0	0	0	0	0	0	0	0	0	0	0	0	0	0	0
	0.75	0	0	0	0	0	0	0	0	0	0	0	0	0	0	0
	1.25	0	0	0	0	**4**	15	19	21	19	16	13	10	8	6	4
	1.75	0	0	0	35	68	75	71	64	55	47	38	31	24	19	15
	2.25	0	0	27	128	146	142	132	120	106	91	76	61	49	39	31
	2.75	2	1	121	216	229	220	203	182	159	137	117	98	81	65	52
	3.25	20	37	212	288	322	305	279	250	221	188	160	134	110	93	77
	3.75	46	120	212	288	339	351	349	320	279	238	203	170	141	120	102
	4.25	85	142	212	288	339	351	345	350	338	285	233	186	149	130	113
	4.75	114	142	212	288	339	351	345	340	350	289	241	196	160	138	118
	5.25	145	142	212	288	339	351	345	340	350	309	262	180	93	110	115
		4.0	**4.9**	**5.7**	**6.6**	**7.5**	**8.3**	**9.2**	**10.0**	**10.9**	**11.7**	**12.6**	**13.5**	**14.3**	**15.2**	**16.0**

Energy Period, Te [sec] $2\pi(m_{-1}/m_0)$

Figure 1-30: BBDB electric power matrix, values displayed in kW. Generator rating of 298kW and VFD rating of 373kW. Shading from scatter diagram maintained to highlight that this device performs best in waves that are not probable.

Figure 1-30 shows the electrical power generated by the system of Figure 1-29 for a VFD power rating of 373 kW, a generator rating of 298 kW. It is interesting to see that the power decrements from the electricity generation equipment are not as large as those incurred by the pneumatic-to-mechanical power conversion equipment. This indicates that the turbine size and vent pressure selection are critical parameters in the optimum PCC design.

Table 1-19 highlights annual estimates for key variables describing the dynamics of the device. As can be seen not only are annual estimates of the power available, but also estimates of device motion. These types of estimates can give the designer a sense for how the device will respond in the deployment climate.

Table 1-19: Annual Estimates of Performance

Variable		RMS (Eq. 13)	Significant (Eq. 14)
Pneumatic Power	kW	207.8	--
Pneumatic Energy Production	MW-hr	1820	--
Capture Width	m	8.89	--
Pressure	Pa	2728	5456
Flow	m^3/sec	66.2	132.5
Heave	m	0.43	0.87
Pitch	deg	2.9	5.7

1.3.4 Array Design

As noted in Section 2.1.1 of the Reference Model Project (RMP) report,[3] due to the scarcity of developed array optimization models, we did not perform detailed array design and analysis as described in the general methodology, and this adds to the uncertainty in the AEP estimate for arrays. In the RM6 wave energy converter analysis, we assumed a maximum of 100 units could be deployed at the reference site in order to take advantage of reduced costs through economies of scale, thus lowering the LCOE estimates. The array layout (number of units and spacing) was estimated based on the bathymetry and the potential installation space available at the deployment site. The estimated required spacing between the devices to accommodate moorings was 800 m. This staggered spacing seeks to minimize the fluid dynamic interaction between devices to ensure that the loss of energy in the array is negligible. [15]

The total array capacity at 100 units is approximately 37 MW (using the VFD rating to determine capacity). For the main cable (cable to shore), we selected a 3-phase AC transmission cable with a voltage level of 30 kilovolts (kV). All transmission cables included fiber optic lines to allow communication from each device to shore. For the RM6 array, groups of 10 devices (only nine are shown in Figure 1-31) are connected with interconnect cables that run between individual units (Figure 1-32). Riser cables transmit electricity via a riser cable to a junction box and a trunk cable connects each junction box. Cable landing is accomplished by directionally drilling a conduit that connects the cable out to the first row of devices. This approach minimizes installation and maintenance costs.

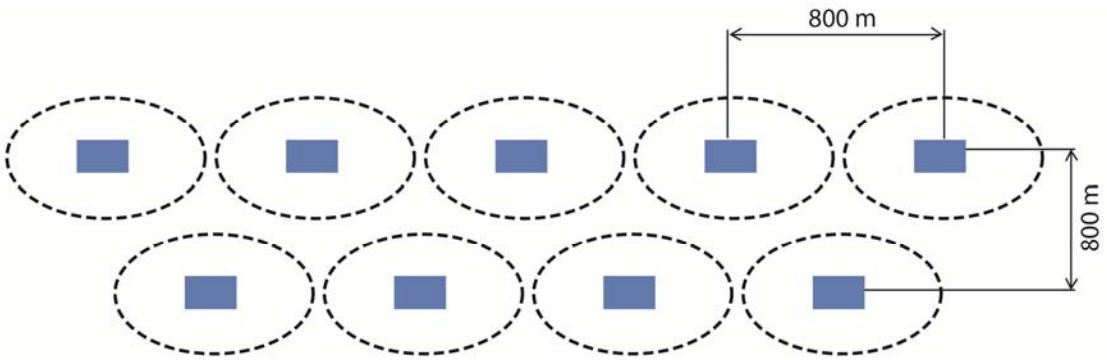

Figure 1-31: Array layout (plan).

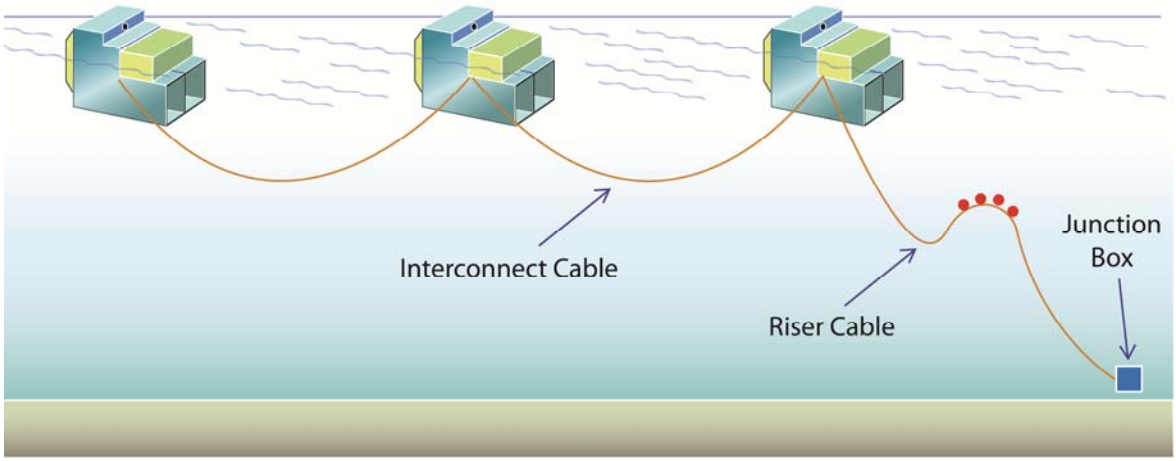

Figure 1-32: Device interconnection cable, riser cable, and junction box (profile). Mooring lines not shown for clarity.

It should be noted that the non-optimized array design presented here provides a starting point for further investigation. Assumptions were made about the size of arrays in order to realize reduced costs from economies of scale. No detailed site analyses for suitable contiguous seabed surfaces were performed. Arrays may, as dictated by the site, be required to include more or less units than the 100 units we assumed. Alternative array designs may incur higher maintenance costs. The mooring of each unit is non-circular, the simplistic staggered array geometry as presented in 1.3.4 may not be optimal. Losses to absorbed power arising from the fluid dynamic interaction between devices are possible and not accounted for in this work.

1.4 Manufacturing and Deployment Strategy

1.4.1 Manufacturing Strategy and Costs

Manufacturing costs of system components for RM6 at different array scales (1, 10, 50 and 100 units) are summarized in the figures and tables below. Figure 1-33 shows the cost breakdown of the device structure subcomponents, which includes the main backward bent duct structure, stern float, bow float and all the girders and structural supports. Nearly 90% of the cost comes from the main structure and additional girders/supports. Approximately 60% of that cost is due to the mass of the girders and structural supports. As mentioned in section 1.3.1, there is an opportunity to reduce mass and therefore reduce the cost of the device by re-evaluating the design of the structure. While there is some reduction due to volume discounts at 100-unit deployment, with a structural mass of approximately 1,800 tonnes a large portion of the cost is due to the price of raw steel.

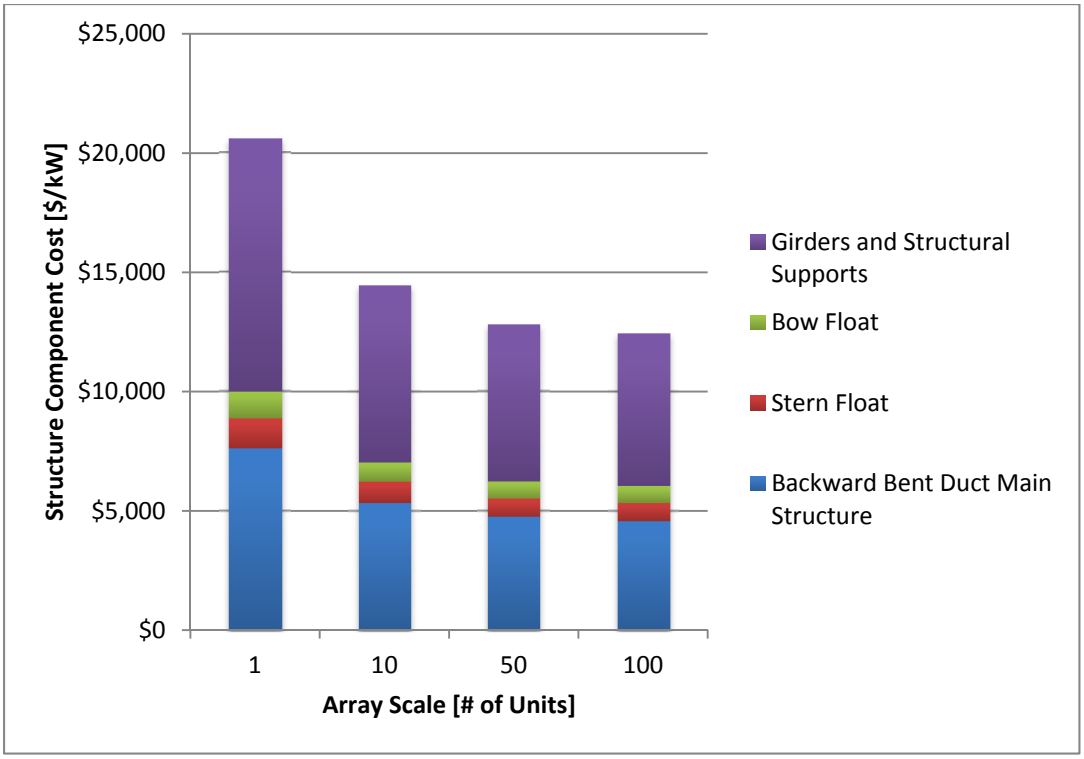

Figure 1-33: RM6 structural cost breakdown ($/kW) per deployment scale.

Figure 1-34 shows cost breakdown for the PCC components of the RM6. ARL estimated the design and manufacturing costs for the wells turbine generator assembly.[44] The greatest contributors to the cost for this PCC system are the fabricated components, which are broken up into circular fabricated components and rectangular fabricated components. Circular fabricated components account for items such as the turbine housing, rotor, power shaft, and nose cone. The circular components make up a large percentage of the PCC mass, and in conjunction with the material loss due to machining it's no surprise that these components make up over 70% of

the PCC cost. While it is outside the scope of this project, the RM6 PCC may benefit from composite materials or advanced manufacturing techniques to reduce the amount of machine time required to fabricate the wells turbine.

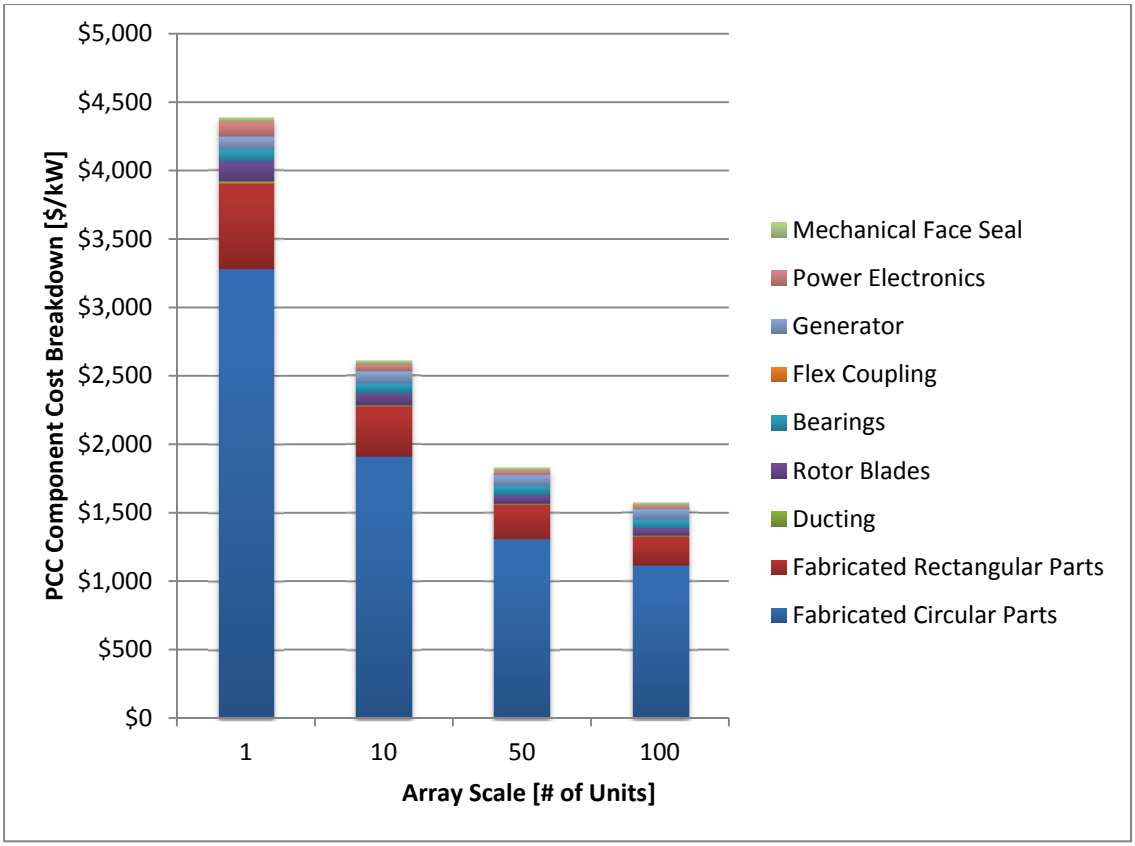

Figure 1-34: Cost breakdown ($/kW) for the PCC components per deployment scale.

Mooring component costs, including: 1) mooring lines and chains, 2) anchors, 3) subsurface buoys, and 4) connecting hardware ready for installation were estimated at approximately $835,000 for a single device deployed as a single unit, or nearly $700,000 per device at a deployment of 100 units. The mooring system costs are dominated by the mooring chains. This is due to the compounding effect of the chain length compared to polyester, as well as the cost per meter of chain compared to polyester. Approximately 38% of the mooring and foundation costs are due to the price of chain. Table 1-20 shows the estimated cost of the components of the mooring system at different deployment scales.

Table 1-20: Mooring system component cost breakdown.

	1-Unit Deployment [$/kW]	10-Unit Deployment [$/kW]	50-Unit Deployment [$/kW]	100-Unit Deployment [$/kW]
Mooring lines/chain	**$1,471**	**$1,324**	**$1,324**	**$1,324**
Polyester Line	$31	$28	$28	$28
R4 Chain	$1,368	$1,231	$1,231	$1,231
Wire Rope to Sub-Sea Buoys	$72	$65	$65	$65
Anchors	**$333**	**$280**	**$224**	**$169**
Buoyancy	**$161**	**$145**	**$145**	**$145**
Connecting Hardware (shackles etc.)	**$274**	**$247**	**$247**	**$247**
Total	**$3,710**	**$3,319**	**$3,264**	**$3,209**

1.4.2 Deployment Strategy and Costs

The deployment strategy for RM6 is similar to that prescribed for Reference Model 3 RM3.[3] It accounts for the installation of the: 1) mooring system, 2) subsea cable infrastructure, and 3) the devices themselves (including commissioning). The RM6 estimate assumes two of the DP-2 class vessels that Re Vision specified for the RM3 installation. The second vessel used for installation is required due to the extra mass of RM6 vs RM3. We assumed that the vessel would be mobilized from the Gulf of Mexico region and used for the mooring installation. A separate Cable Installation Vessel would be used for installing the cable. The device[1] would be connected to its mooring system and commissioned using the same workboat/custom service vessel that will be used for O&M activities. The vessel quoted for the RM3 mooring installation has a deck area that is limited to 2-3 RM3 mooring lines per trip. Due to the increased length and mass of the RM6 mooring lines, it was assumed that a similar vessel would be used but the installation time would increase by 50%.

Table 1-21 lists the total installation costs using the assumed day rates for these three types of vessels and the assumed installation durations for the key steps in the installation process.

[1] This analysis assumed devices could be assembled in a suitable fabrication facility in Oregon and barged down to the installation site about 300 miles south.

Table 1-21: RM6 M&D Strategy Module cost assumptions.

Operation Detail	1-Unit			10-Unit		
	No. Days	Vessel Day Rate	Cost	No. Days	Vessel Day Rate	Cost
Mooring Installation (DP-2 Vessel)						
Transit (5,000 miles)	68.7	$58,754	$4,039,062	68.7	$58,754	$4,039,062
Mob/Demob of Vessels	4.0		$422,000	4.0		$422,000
Dockside Support			$7,350			$73,500
At Dock Landing	0.4	$70,485	$26,079	3.7	$70,485	$258,445
Transit to Site and back	0.4	$76,610	$27,580	3.6	$76,610	$275,796
On-Site working	0.4	$73,810	$27,310	3.7	$73,810	$270,637
Total	**74**	**$279,659**	**$4,549,381**	**84**	**$279,659**	**$5,339,440**
Cable Shore Landing						
Horizontal Drilling			$667,000			$767,200
Cable Installation (Using Cable Install Vessel)						
Mob/Demob CIV	11.0	$66,350	$729,850	11.0	$66,350	$729,850
Load Cable	0.7	$75,625	$53,694	3.4	$75,625	$257,125
Transit to Site	2.0	$101,275	$202,550	2.0	$101,275	$202,550
Install Cable & Surface Lay	0.6	$101,075	$55,591	5.5	$101,075	$555,913
Cable Burial and S/E	3.1	$101,075	$313,333	3.1	$101,075	$313,333
Contingency	1.7	$87,855	$152,516	0.0	$0	$0
Total	**19**	**$533,255**	**$1,507,534**	**25**	**$445,400**	**$2,058,770**
Device Installation (Same Workboat used for O&M)						
Mob/Demob			$181,750			$181,750
Installation	1.0	$133,550	$133,550	10.0	$133,550	$1,335,500
Contingency	0.1	$133,550	$13,355	1.0	$133,550	$133,550
Total	**1**	**$267,100**	**$328,655**	**11**	**$267,100**	**$1,650,800**

Figure 1-35 shows the total installation cost normalized by installed power at different deployment scales. The single unit deployment cost is dominated by the cost to install the mooring system and the cable shore landing. The installation cost, in terms of $/kW, is significantly higher for the deployment of a single unit as compared to an array (even arrays with only 10 units). The dollars per-kW cost of installation is estimated to fall from about $16,000/kW for a single unit deployment, to approximately $2,500/kW for a 10-unit deployment, and just over $1,000/kW for a 100-unit deployment. The device capacity has a significant effect on the installation costs, this translates to a lower $/kW cost for RM6 than RM3 despite the higher capital cost.

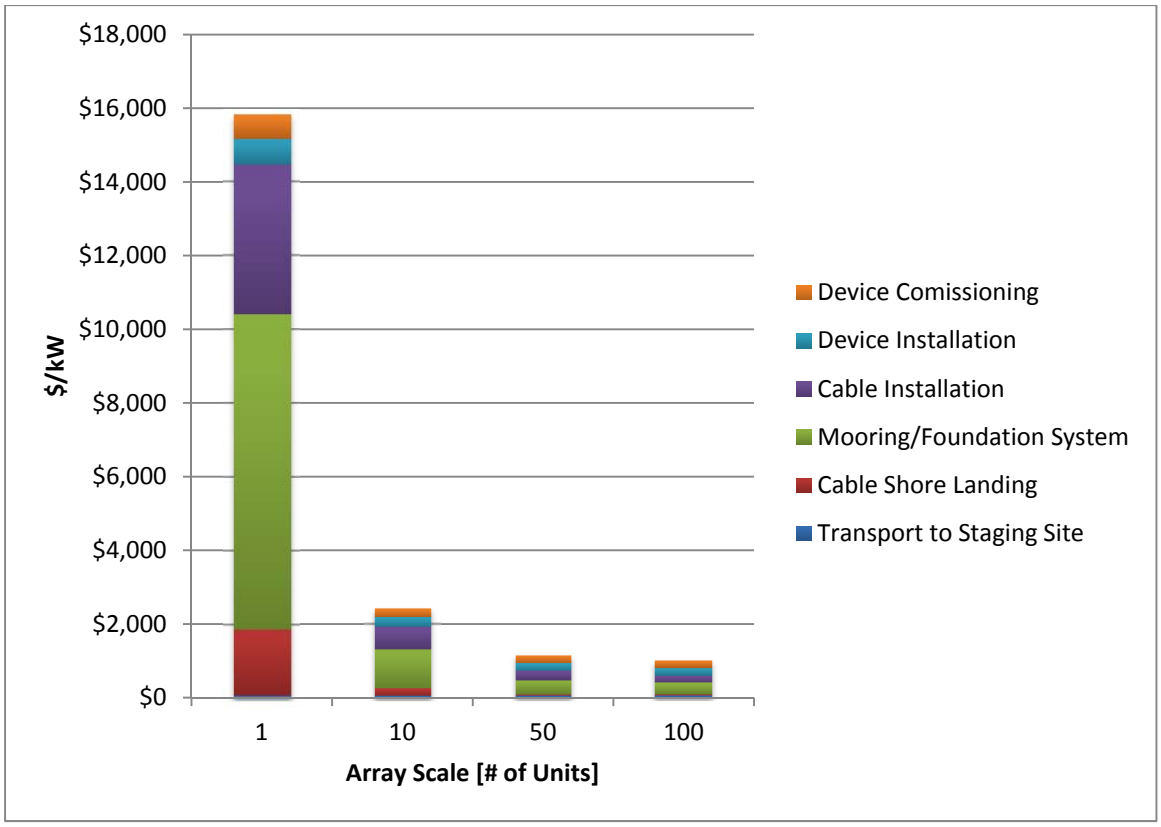

Figure 1-35: Installation cost breakdown ($/kW) per deployment scale.

1.5 Operations and Maintenance Strategy

1.5.1 Service Vessel Specifications

Similar to RM3, it was assumed that a dedicated service vessel will become feasible at larger unit deployment. The workboat specified for RM3 would likely be sufficient for typical service intervals. The boat shown in Figure 1-36, represents a small offshore supply/workboat in the 85-125 ft. range. The requirements for the vessel were: 1) sufficient deck-space to handle mooring lines and cable repair; 2) dynamic positioning (DP-1) to allow for more effective operation; and 3) crane lifting capacity of 5 Mg at 20-foot radius. Total cost estimates for the RM3 vessel were on the order of $4M to $5.5M assuming it was built new. The conservative estimate of $5.5M was used for the larger deck space required to accommodate the longer RM6 mooring system. A 10-person crew, approximately, would be required to operate the vessel and carry out repair and maintenance activities. Operations would take place only during daylight hours (12-hours per day) and the vessel would return to port at night.

Figure 1-36: General type of medium sized workboat.

NOTE: Refer to www.sunmachinery.com/workboats_for_sale.html for this and other workboat images.

The cost of marine operations is based on the number of interventions and the cost of the vessels used for operations.

Based on the failure rate assumptions (see next section) and operational frequency, it was found that the device would require a total of two interventions per year. There are two major types of interventions: those requiring device recovery and those requiring only PCC recovery. The vessel day rates are the same for both types of interventions with the exception of the cost of fuel and consumables; the rate is higher for device retrieval. Similar to installation, it is assumed that device retrieval would require two vessels compared to the single vessel used in RM3. The operational cost would be expected to drop if the WEC farm used a custom-built service vessel that is purchased as part of the project rather than employing a vessel of opportunity.

1.5.2 Failure Rates

Table 1-22 provides first order approximations of failure rates based on failure rates estimated for RM3. Failure rate approximations for the Wells Turbine were made from the report by Thorpe, 1992.[45] The L-50 life was assumed to be the mean-time of the subsystem requiring complete replacement. Only components that would not require complete device retrieval were considered for replacement. The cost of replacement parts was assumed to equal the value of the part/subsystem of the original device. Annual replacement part costs were calculated from the part cost and the estimated number of failures per year (Table 1-22).

Table 1-22: Cost and failure rate assumptions for WEC components (single unit cost).

Wells Turbine Assembly		$/Unit	# Units	L50	$/Year	# Failures/Year
	Rotor Blades	3,738	5	8	2,336	0.13
	Bearings	4,007	6	10	2,404	0.10
	Flex Couplings	996	1	10	100	0.10
Electrical Systems						
	Generator	27,245	1	10	2,724	0.10
	Power Electronics	8,933	1	7.5	1,191	0.13
External Systems						
	Riser Cable	110,000	1	10	11,000	0.10
	Moorings	703,000	1	50	14,060	0.02
Total					**33,815**	**0.68**

NOTE: The values in the table are for a 100-unit project.

1.5.3 Annual O&M Costs

Based on the estimated number of interventions and replacement part values, the annual O&M cost was computed at different scales of deployment.

Figure 1-37 shows the breakdown of the likely annual cost per WEC device. Increasing the unit scale of the farm would greatly reduce operational costs because the costs for the service vessel (and the number of the crew) would increase at a lower rate as the deployment scale goes up. Insurance estimated for RM3 were adopted for RM6, which is a percentage of the summation of Infrastructure, Mooring/Foundation, Device Structure, PCC, Subsystem Integration, and Installation costs. It is assumed that for single and 10-unit deployment insurance is 2%, 1% for 50-units, and 0.5% for 100-units. Note that the post-installation monitoring is a part of environmental monitoring and regulatory compliance costed under the Environmental Compliance (EC) Module (see Section 1.3.7) and is included in the total OpEx costs shown in Figure 1-37. Initial environmental compliance and monitoring activities prior to start up would fall under CapEx as explained in the following section.

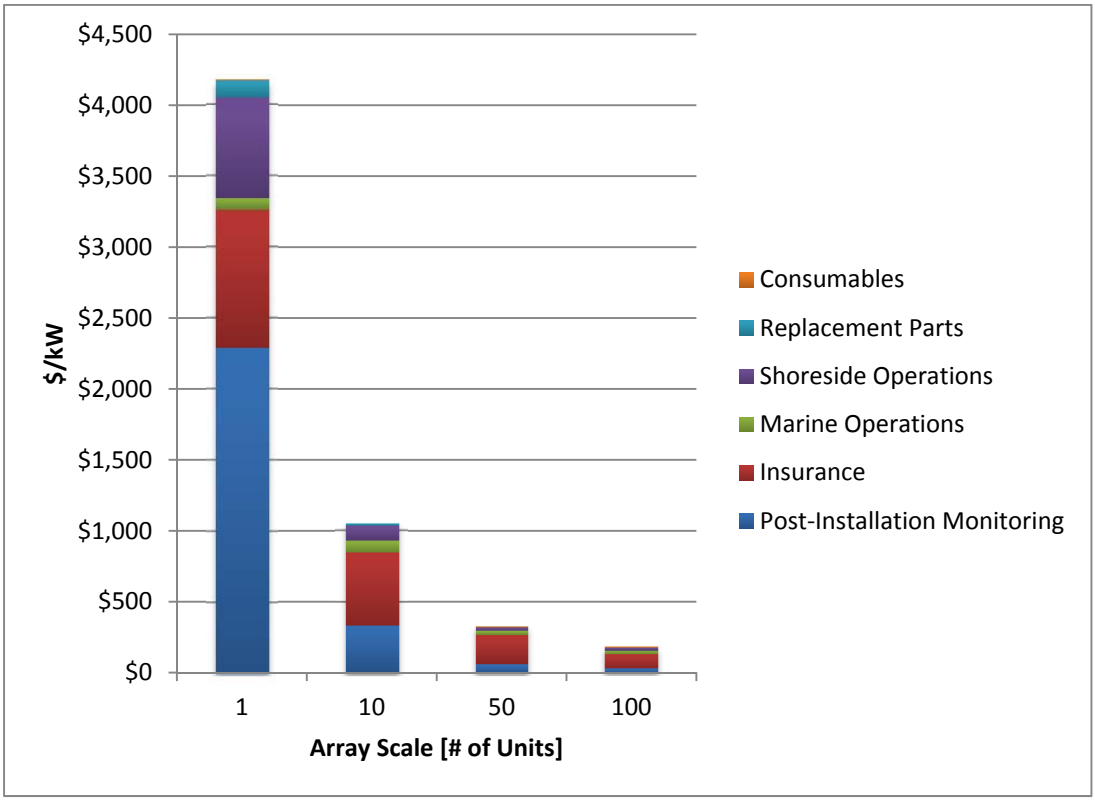

Figure 1-37: Annual OpEx cost ($/kW) per array size.

1.6 Environmental Compliance

Responsible deployment of marine and hydrokinetic (MHK) devices in estuaries, coastal areas, and major rivers requires that biological resources and ecosystems be protected through siting and permitting (consenting) processes. Scoping appropriate deployment locations, collecting pre-installation (baseline) and post-installation data all add to the cost of developing MHK projects, and hence to the cost of energy. Under the direction of the U.S. Department of Energy, Pacific Northwest National Laboratory scientists have developed logic models that describe studies and processes for environmental siting and permitting as laid out in the Reference Model Project (RMP) report.[3], [46],[47] The logic models and all costing information are separated into four stages: NEPA and administrative process, siting and scoping, pre-installation assessment, and post-installation monitoring.

For RM6, the basis for costs of environmental studies and processes were developed through extrapolation from the previous three models, relying heavily on costing for RM3 (WEC point absorber). Both RM3 and RM6 are wave energy converters with some potential for commonalities in interactions with receptors of concern. The impact of anchors and mooring lines on marine habitats are somewhat analogous for both RM3 and RM6. The ocean space occupied by RM6 is similar to RM3 and NEPA processes and study costs can be extrapolated using PNNL staff knowledge of other MHK projects and from consultation with experts in the area.[48] In the context of potential environmental interactions which affect study costs, the primary differences between RM3 and RM6 are in the much larger surface expression of RM6 (35 m length, 27 m width, rising 10 m above the water line), the presence of large air chambers below the surface (17.5 m length, 27 m width), and the use of an air turbine for the power take off.[3]

The overall costs for environmental studies and associated processes required for RM6 are summarized in Table 1-23. Detailed spreadsheets, references, standardized protocols, and in-depth explanation of costing is available for all parts of the environmental costing process for RM6.[46],[47] It should be noted that the costs listed here are not intended to make recommendations for which studies should be carried out or how much they should cost, but rather to reflect cost data representative of projects carried out to date, coupled with professional judgment on how costs associated with RM6 may differ over project scales. Project-specific costs may be significantly lower or higher depending on the project's specific site characteristics, regulatory concerns, and stakeholder dynamics. Costs are also expected to come down over time. Numbers here represent a conservative estimate, and are not intended to inform study plan negotiations between developers and regulatory agencies.

Table 1-23: RM6 environmental cost summary.

Information Need	Pilot		Small Scale Commercial		Large Scale Commercial	
	Low	High	Low	High	Low	High
Siting & Scoping	$240,000	$390,00	$330,00	$530,00	$330,00	$530,00
Pre-Installation Studies	$1,218,000	$2,047,00	$1,753,00	$3,452,00	$2,233,00	$4,537,00
Post-Installation	$660,000	$1,050,00	$9,355,00	$19,800,00	$10,705,00	$24,150,00
NEPA & Process	$800,000	$1,400,00	$1,100,00	$2,300,00	$1,300,00	$2,550,00
Total	$2,918,000	$4,887,00	$12,538,00	$26,082,00	$14,568,00	$31,767,00

Costs shown here summarize **total** costs expected at pilot and each commercial phase. As described more fully below, commercial costs were extrapolated from pilot costs under the assumption that information collected during permitting at the pilot scale will be used for permitting at the commercial phase as well, thereby achieving cost savings. Commercial costs were calculated as incremental costs above those incurred in the pilot; to construct Table 1-23, commercial costs were added to the pilot costs to produce the total cost for both small-scale and large-scale commercial phases.

Using data from representative pilot project study plans, the studies that are likely to be required were derived for each reference model stage; costs were then estimated for each study. The required studies and associated costs were based on assumptions derived from project experience and expert opinion. Examples of the studies and the assumptions driving these costs are shown in Table 1-24. Cost ranges were used to represent the breadth of studies that may be required, depending on the specific animals and habitats encountered in the deployment area, as well as the range of materials, personnel, and equipment available. For example, if no endangered small cetaceans (i.e., dolphins, porpoises, killer whales) were found near the project site, the marine mammal surveys costs would be reduced to focus only on the presence of large cetaceans (i.e., the great whales). If a university partner or non-profit were capable of carrying out the work, costs might be less than those to employ a private firm. Conversely, if new instrumentation must be developed and tested expressly for the projects, costs may be higher.

Table 1-24: Examples of pilot scale study assumptions for RM6 – pre-installation (baseline) studies for fish, marine mammals, seabirds, and turtles.

Information Need	Specific Studies	Key Assumptions
Marine mammals	Baseline—species abundance, distribution, and behavior: acoustic monitoring; and literature review.	One year study. Large vessel for gray whale surveys in spring and winter; small vessel surveys for resident gray and humpbacks in summer and fall; acoustic monitoring with autonomous recorders for other species (i.e., dolphins and porpoises). This includes boat time to set and retrieve recorders.
Fish and invertebrates	Baseline—species abundance, distribution, and behavior for sturgeon, invertebrates (including crabs), and fish.	Two years of pre-installation monitoring as required by agencies; 1) Telemetry receivers to detect tagged ESA-listed sturgeon; 2) Grab sampling to assess benthic invertebrates; 3) Trapping to assess Dungeness crab; 4) Trawling to assess demersal fish and benthic invertebrates
Birds	Baseline—species abundance, distribution, and behavior	Small boat surveys and line transects for 1 year; Low estimate: assumes 6 surveys done in conjunction with marine mammal surveys, 6 done independently. High estimate: assumes 24 surveys/year done independently.
Sea turtles	Baseline— species abundance, distribution, and behavior for ESA-protected turtles in project area	One year of surveys. Low estimate: surveys done in conjunction with marine mammal and seabird boat surveys, no equipment charges; High estimate- surveys done from small aircraft

Factors such as waterbody characteristics, MHK technologies, and the marine animals and habitats indigenous to the site will be reflected in differences among permitting and siting costs for MHK projects in the U.S. As more MHK sites are chosen for development, additional permitting requirements and siting complexities may arise causing even greater divergence in permitting and siting costs.

The reference site for the OWC RM6 is located in approximately 50 meters of water in a coastal Northern California location, similar to RM3. Extensive pre- and post- installation monitoring will be needed to better understand the interaction between this device and migratory marine

mammals, fish and reptiles; endangered species like the gray whale, Stellar sea lion, Chinook salmon, and green sturgeon will inhabit this coastal environment during their migratory routes and for feeding. RM6 differs from RM3 (WEC Point Absorber) in several significant ways: the very large superstructure of the OWC may act as an attraction to birds; the air turbine above the water may have acoustic impacts (105-140 dB) on wildlife or potentially present a nuisance to recreational users of the area; the presence of large air chambers beneath the device could potentially present an entrainment risk to fish, marine mammals, or diving birds; and finally, long mooring lines (two 810-meter lines port and starboard, and one 200-meter line aft, arranged in a three-point mooring) may present a greater risk to habitat from dragging or present a risk of fishing gear entanglement, that may in turn endanger fish, marine mammals, diving birds, sea turtles and some invertebrates. Finally, the devices are much larger than a typical point absorber buoy, and an array of 50+ devices would require considerably more space than a similar sized array of RM3 devices. Greater site dimensions are likely to increase the area of potential environmental effects and drive higher survey and monitoring costs.

1.7 LCOE Calculation

The baseline commercial LCOE estimate (i.e., an array comprised of 10 units) for the RM6 device is $1.98/kWh. This value is based on the FCR, AEP, CapEx, and OpEx estimates shown in Figure 1-38. Based on these values it's critical that the device cost must decrease for this technology to become economically viable. The AEP for a 100-unit array was estimated to be 90,400 MWh per year, which is approximately 20% higher than the RM3. Similarly to RM3 there is a significant effect of economies of scale at larger deployment scales. However, the 20% increase in AEP isn't enough to offset the structural cost associated with the current RM6 design. Figure 1-38 shows a breakdown of high level LCOE at 4 different deployment scales. Table 1-25 gives a detailed breakdown for a commercial deployment of 10-units. The cost of manufacturing and deployment contributes 53.2% of the total LCOE for RM6, and 70% of the M&D cost is due to the cost of the device structure. This suggests that there is potential to reduce the LCOE of this device by either increasing AEP or decreasing the structural cost.

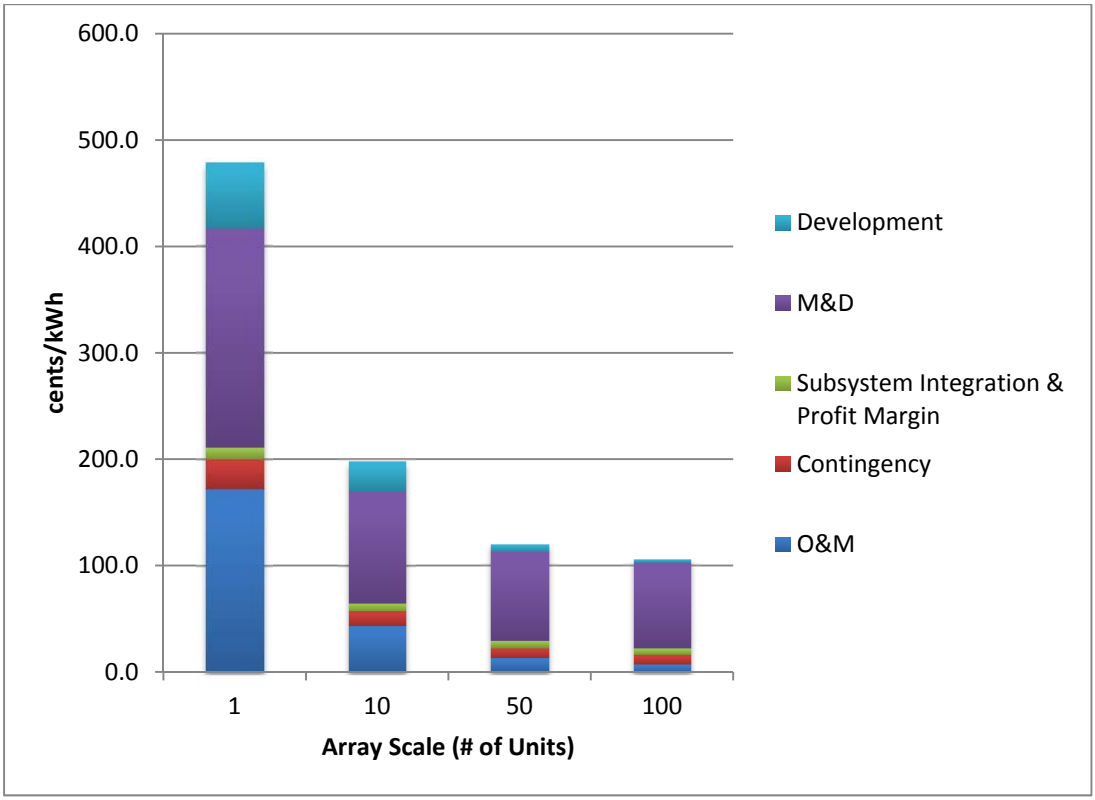

Figure 1-38: High-level LCOE (cents/kWh) breakdown per deployment scale for RM6.

Table 1-25: RM6 LCOE breakdown by cost category (10-unit array).

	cents/kWh	% of Total LCOE
Development	27.5	13.9%
M&D	105.3	53.2%
Subsystem Integration & Profit Margin	7.6	3.8%
Contingency	14.0	7.1%
O&M	43.5	22.0%
Total	198.0	100.0%

The total CapEx for single unit deployment was estimated to be approximately $69,000/kW, but this value drops to $34,650/kW for 10-unit deployment. While there are some costs savings associated with volume production in items such as the PCC, the largest reductions are due to installation and permitting. Due to the large structure mass there isn't a significant reduction in device structural component cost from 1-unit to 10-unit or to 100-unit production. Figure 1-39 shows the contribution of CapEx to the RM6 LCOE.

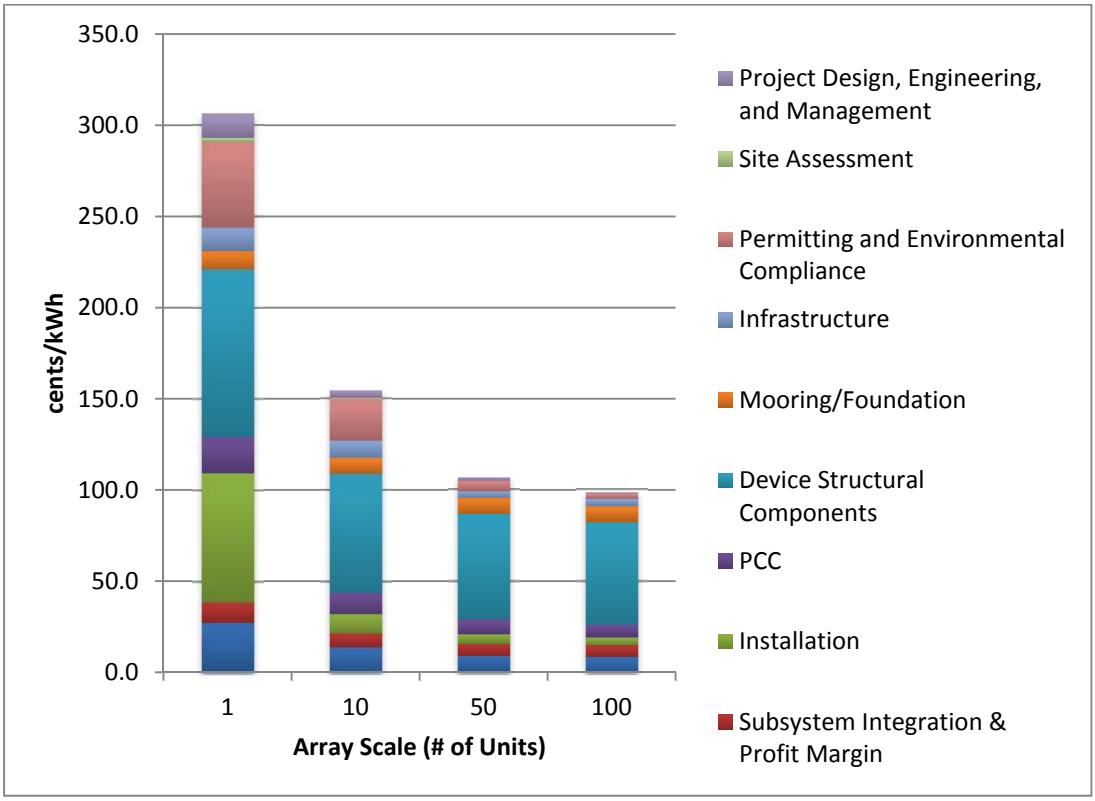

Figure 1-39: RM6 CapEx contributions to LCOE (cents/kWh) per deployment scale.

The detailed breakdown CapEx cost categories in terms of LCOE, as well as the percentage breakdown is provided in Table 1-26 for a 10-unit array.

Table 1-26: Breakdown of RM6 CapEx contributions to LCOE (10-unit array).

	cents/kWh	% of Total CapEx
Design	4.1	2.6%
Site Assessment	0.4	0.2%
Permitting and Environmental Compliance	23.0	14.9%
Infrastructure	9.4	6.1%
Mooring/Foundation	8.9	5.8%
Device Structural Components	64.6	41.8%
PCC	11.7	7.5%
Installation	10.9	7.0%
Subsystem Integration & Profit Margin	7.6	4.9%
Contingency	14.0	9.1%
Total	154.5	100.0%

Annual operating cost was estimated at $4,180/kW for a single unit and $1054/kW for 10-unit array. Similarly to how the CapEx costs were shown, Figure 1-40 shows how OpEx costs contribute to the RM6 LCOE.

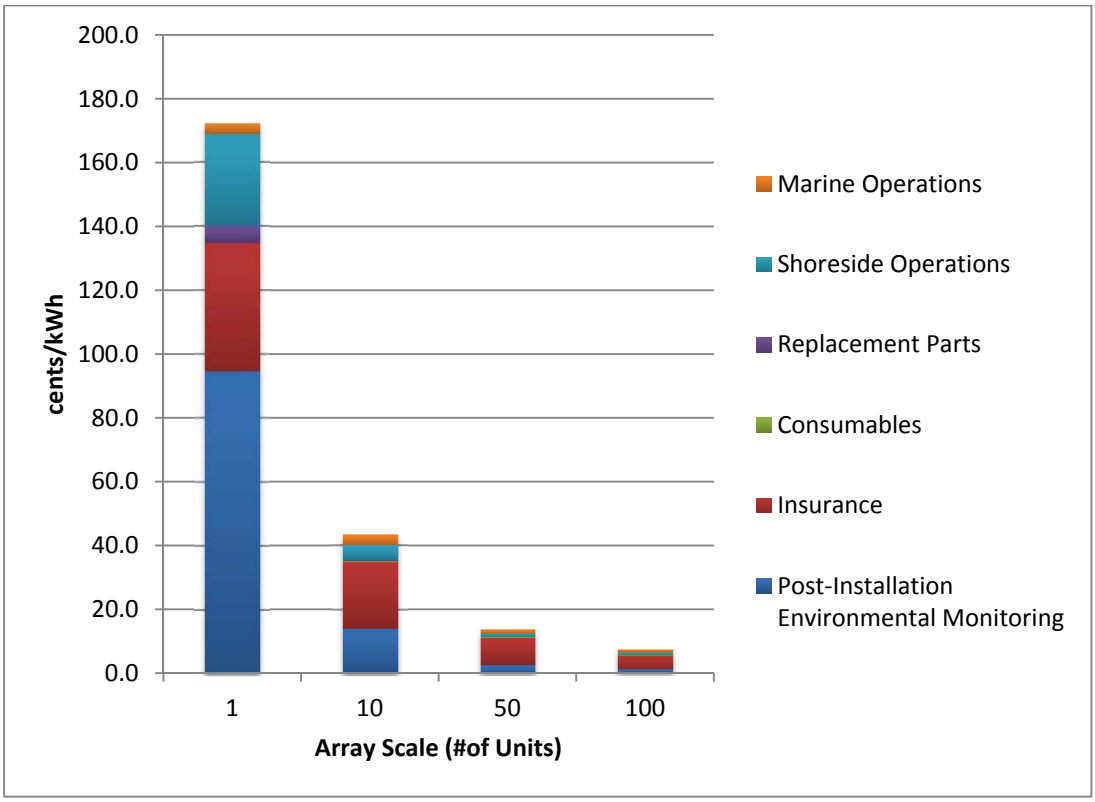

Figure 1-40: RM6 OpEx contributions to LCOE (cents/kWh) per deployment scale.

A detailed breakdown of the RM6 OpEx contributions to LCOE is provided for a 10-unit array in Table 1-27.

Table 1-27: Breakdown of RM6 OpEx contributions to LCOE (10-unit array).

	cents/kWh	% of Total OpEx
Marine Operations	3.47	8.0%
Shoreside Operations	4.42	10.2%
Replacement Parts	0.47	1.1%
Consumables	0.22	0.5%
Insurance	20.91	48.1%
Post-Installation Environmental Monitoring	14.00	32.2%
Total	43.50	100.0%

1.7.1 CapEx and OpEx uncertainties

Due to the lack of WEC devices installed in the United States there are uncertainties around all the proposed Reference Model devices. While there are OWC's installed in other parts of the world, reliable operational data on floating OWC's is currently unavailable. A qualitative assessment of uncertainty for CapEx is shown in Table 1-28, and the assessment for OpEx is shown in Table 1-29. A more detailed description of the uncertainties is given below:

- **Development:** PNNL has performed an initial study on the environmental compliance, however post-installation monitoring has considerable uncertainty. Aside from post-installation monitoring the costs associated with monitoring are dependent upon the site location and final array size. Until a pilot device is installed there will be uncertainty with the selected design which leads to a medium to high level of uncertainty.
- **Infrastructure:** Costs estimates for cables and connections were obtained based on previous reference model work. Adjustments were made for the additional spacing between devices, and therefore are considered to have a medium level of uncertainty. There is a high uncertainty with the vessel estimates due to the uncertainty of the hydrodynamic drag associated with the current RM6 design. Conservative cost estimates have been utilized and it is likely these costs can be optimized in future designs.
- **Foundation/Mooring:** There is a low to medium level of uncertainty in the foundation and mooring estimates due to the analytical design and simulations performed. The results of these simulations allowed for more detailed costs estimates that assume shipping to the site location.
- **Device Structural Components:** A high level of uncertainty on the device structure is due to the uncertainty around the final design. As mentioned section 1.3.1 it is likely that the design is overly conservative and therefore may have significant potential to reduce cost. There is less uncertainty in the methods used to estimate the costs of the design. Fabricated steel costs similar to what was used on RM3 were used to estimate costs for the RM6 structure.
- **Power Conversion Chain:** There is a low level of uncertainty with the power conversion chain due to the wells turbine/generator set being designed and priced out at the component level.

- **Installation:** Installation estimates are based on time and material (vessels included) estimates. There is uncertainty around the specific vessels used during installation and therefore installation has been assigned a medium to high level of uncertainty.
- **Subsystem Integration & Profit Margin:** There is a high level of uncertainty due to a simple 10% factor added on to the device cost.
- **Contingency:** There is a high level of uncertainty due to a simple 10% factor added on to the device cost.
- **Decommissioning:** Decommissioning costs are assumed to have equivalent costs associated with Installation and therefore are ranked as a medium level of uncertainty.
- **Marine Operations:** There is a high level of uncertainty due to a simplified O&M model.
- **Shoreside Operations:** There is a high level of uncertainty due to a lack of long term performance data associated with wells turbine reliability. This leads to an uncertainty in failure rates and required maintenance salary.
- **Replacement Parts:** Replacement part cost is based on original part cost. The high level of uncertainty is due to an uncertainty in failure rates for wells turbines and their components.
- **Consumables:** There is a high level of uncertainty around the consumables required for the wells turbine generator and wells turbine lubrication requirements.
- **Insurance:** Insurance is based on knowledge gained from Oil/Gas and offshore wind projects and therefore there is a low level of uncertainty.
- **Post Installation Environmental Monitoring:** The analysis performed by PNNL leads to a low to medium level of uncertainty. The uncertainty will certainly be higher if a different location was selected.

1.7.2 Sensitivity Analysis: OWC Weight

As identified above, the weight of the BBDB is primary driver of the high LCOE. Hence a small sensitivity analysis has been completed to understand the effect on the LCOE. Figure 1-41 shows the dependence of the LCOE on the structural mass. This analysis only takes into account the mass directly, it does not account for the savings that could be possible due to the reduced mass (e.g. smaller deployment vessels, smaller lifting cranes, etc.).

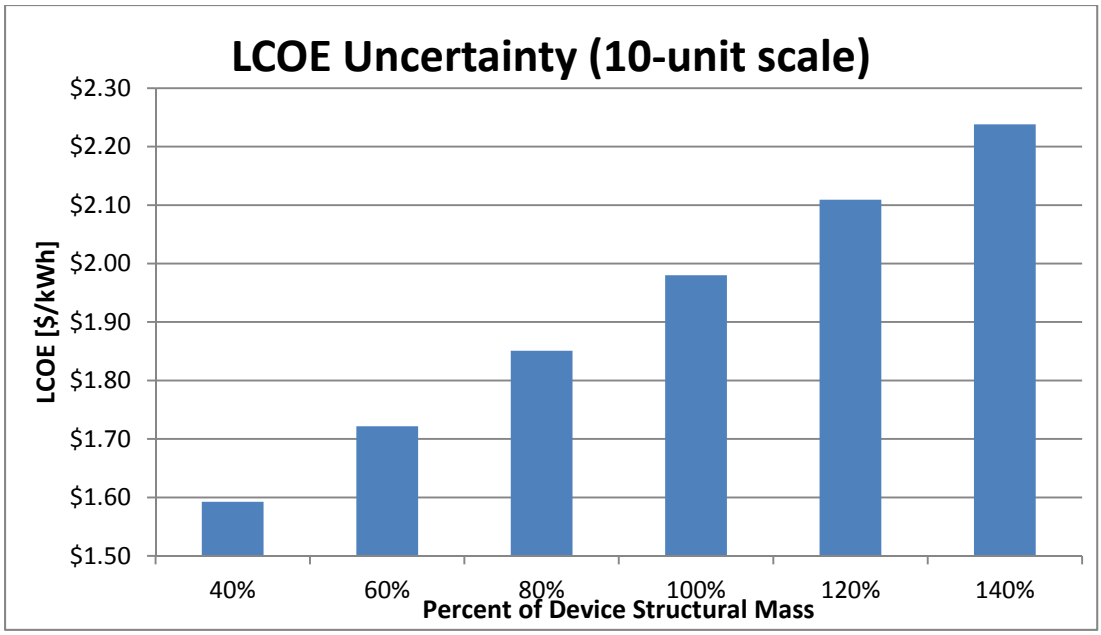

Figure 1-41: LCOE uncertainty in the RM6 BBDB device.

It is possible that the structural mass could be as low as 40% of the 1,809 metric tonnes presented here, i.e. closer to 724 metric tonnes. Clearly this has a huge effect on the LCOE of this device changing it from $1.98/kWhr to $1.59/kWhr. For evaluation, the RM3 device was calculated to be 680 metric tonnes and had an estimated LCOE of $1.45/kWh for a 10 unit array.[3]

This analysis is presented to highlight that the initial LCOE value presented in this report could be inflated by up to 20%.

Table 1-28: Assessment of Cost Uncertainty (CapEx)

CBS Category	Sub-Category (if Applicable)	Result Maturity / Fidelity	Uncertainty
Development	Siting and Scoping Pre-Installation Studies Post-Installation Studies NEPA & Process Site Assessment	Based on data from similar studies and/or engineering judgment and/or data from PNNL study.	Medium to High
	Design and Engineering	TRL 3 design and analysis	High
Infrastructure	Cables and Connectors	Conceptual layout, generic hardware ID and estimates	Medium
	Dockside and Vessel	Generic for dockside and Generic vessel ID	High
Foundation/ Mooring	N/A	Design with Combination of specific and conceptual hardware	Low to Medium
Device Structural Components	All	CAD designs, Conceptual Designs, steel cost estimates. High uncertainty is due to potential for re-design.	High
PCC	All Components	ARL designed turbine with fabrication estimates and off the shelf part quotes	Low
Installation	N/A	Time and Material estimates for a specific resource location which includes labor	Medium to High
Subsystem Integration & Profit Margin	N/A	Assumed to 10% of machine cost	High
Contingency	N/A	Assumed to 10% of machine cost	High
Decommissioning	N/A	Assumed to be same as installation cost	Medium

Table 1-29: Assessment of Cost Uncertainty (OpEx).

CBS Category	Sub-Category (if Applicable)	Result Maturity / Fidelity	Uncertainty
Marine Operations	N/A	Large Uncertainties with respect to maintenance and a simplified O&M model	High
Shore-side Operations	N/A	Large Uncertainties in failure rates due to lack of Wells turbine performance data	High
Replacement Parts	N/A	Limited failure rate data, based on original part cost	High
Consumables	N/A	Assumed value for lubrication and other consumables	High
Insurance	N/A	Based on offshore Oil/Gas projects	Low
Post-Installation Environmental Monitoring	N/A	Based on PNNL study	Low to Medium

REFERENCES

[1] Y. Masuda, T. Yamazaki, Y. Outa, and M. McCormick, "Study of Backward Bent Duct Buoy," in *OCEANS '87*, 1987, pp. 384–389.

[2] D. Bull and E. Johnson, "Optimal Resistive Control Strategy for a Floating OWC Device," in *Proceedings of the 10th European Wave and Tidal Energy Conference*, Aalborg, Denmark, 2013.

[3] V. Neary, M. Previsic, R. Jepsen, M. Lawson, Y.-H. Yu, A. Copping, A. Fontaine, K. Hallett, and D. Murray, "Methodology for Design and Economic Analysis of Marine Energy Conversion (MEC) Technologies," Sandia National Laboratories, Sandia Report SAND2013-9040, Mar. 2014.

[4] G. Copeland, D. Bull, R. Jepsen, and M. Gordon, "Oscillating Water Column Structural Model," Sandia National Laboratories, SAND Report SAND2014-18082, Sep. 2014.

[5] D. Bull and P. Jacob, "Methodology for creating nonaxisymmetric WECs to screen mooring designs using a Morison Equation approach," in *OCEANS '12. "Harnessing the Power of the Ocean". Proceedings*, Hampton Roads, VA, 2012, pp. 1 –9.

[6] D. Bull and D. Brefort, "Mooring Design for the Floating Oscillating Water Column Reference Model," Sandia National Laboratories, SAND Report SAND2014-17817, Sep. 2014.

[7] D. Bull, "Pneumatic Performance of a Non-Axisymmetric Floating Oscillating Water Column Wave Energy Device in Random Waves," in *Proceedings of the 2nd Marine Energy Technology Symposium*, Seattle, WA, USA, 2014.

[8] D. Bull, B. Gunawan, and B. Holmes, "Experimental Confirmation of Water Column Natural Resonance Migration in a BBDB Device," Sandia National Laboratories, SAND Report SAND2014-17816, Aug. 2014.

[9] C. Smith, D. Bull, S. Willits, and A. Fontaine, "Optimization and Annual Average Power Predictions of a Backward Bent Duct Buoy Oscillating Water Column Device using the Wells Turbine," presented at the 7th annual Global Marine Renewable Energy Conference: Marine Energy Technology Symposium, Seattle, WA, USA, 2014.

[10] C. Smith, S. Willits, D. Bull, and A. Fontaine, "Optimization and Annual Average Power Predictions of a Backward Bent Duct Buoy Oscillating Water Column Device Using the Wells Turbine," Sandia National Laboratories, SAND Report SAND2014-1689R, Jul. 2014.

[11] B. P. Dooher, E. Cheslak, R. Booth, D. Davy, A. Faraglia, I. Caliendo, G. Morimoto, and D. Herman, "PG&E WaveConnect Program Final Report," Pacific Gas and Electric Company, 2011.

[12] J. C. Berg, "Extreme Ocean Wave Conditions for Northern California Wave Energy Conversion Device," *Sandia Natl. Lab. Doc. SAND2011-9304*, 2011.

[13] Det Norske Veritas, "Position Mooring," Offshore Standard DNV-OS-E301, Oct. 2010.

[14] "SWAN - Simulating Waves Nearshore Cycle III, Version 41.01." [Online]. Available: http://swanmodel.sourceforge.net/. [Accessed: 10-Sep-2014].

[15] A. Babarit, "A review of the park effect in arrays of Wave Energy Converters," in *4th International Conference on Ocean Energy*, Dublin, Ireland, 2012.

[16] I. Imai, K. Toyota, S. Nagata, T. Setoguchi, and M. Takao, "An experimental study on generating efficiency of a wave energy converter Backward Bent Duct Buoy," presented at the European Wave and Tidal Energy Conference, Southampton, UK, 2011.
[17] M. Suzuki, T. Kuboki, S. Nagata, and T. Setoguchi, "Numerical Investigation of 2D Optimal Profile of Backward-Bent Duct Type Wave Energy Converter," *J. Offshore Mech. Arct. Eng.*, vol. 133, no. 4, pp. 041602–8, Nov. 2011.
[18] D. Hong, S. Hong, and S. Hong, "Numerical study on the reverse drift force of floating BBDB wave energy absorbers," *Ocean Eng.*, vol. 31, no. 10, pp. 1257–1294, 2004.
[19] Ocean Energy Ltd., "Ocean Energy OEBuoy: A Backward Bent Duct Design." [Online]. Available: http://www.oceanenergy.ie/. [Accessed: 04-Apr-2013].
[20] Kurniawan, A, Hals, J, and Moan, Torgeir, "Modeling And Simulation Of A Floating Oscillating Water Column," in *Proceedings of the ASME 2011 30th International Conference on Ocean, Offshore and Arctic Engineering*, Rotterdam, The Netherlands, 2011.
[21] D. N. Veritas, "Hull structural design ships with length 100 metres and above." 2009.
[22] *WAMIT v7.0*. Chestnut Hill, Massachusetts: WAMIT, Inc.
[23] T. Whittaker and M. Folley, "Optimisation of wave power devices towards economic wave power systems," presented at the World Renewable Energy Congress, Aberdeen, Scotland, 2005.
[24] "Anchor Manual 2010: The Guide to Anchoring," Vryhof Anchors, 2010.
[25] R. J. A. R. A. F.de O Falcão, "Stochastic modelling of OWC wave power plant performance," *Appl. Ocean Res.*, no. 2, pp. 59–71, 2002.
[26] D. V. Evans, "The Oscillating Water Column Wave-energy Device," *IMA J. Appl. Math.*, vol. 22, no. 4, pp. 423–433, Dec. 1978.
[27] D. V. Evans, "Wave-Power Absorption by Systems of Oscillating Surface Pressure Distributions," *J. Fluid Mech.*, vol. 114, pp. 481–499, 1982.
[28] A. J. N. A. Sarmento and A. F. de O. Falcão, "Wave generation by an oscillating surface-pressure and its application in wave-energy extraction," *J. Fluid Mech.*, vol. 150, pp. 467–485, 1985.
[29] Lee, C.-H., Newman J.N., and Nielsen F.G., "Wave interactions with an oscillating water column," in *Proceedings International Offshores and Polar Engineering Conference*, Los Angeles, 1996.
[30] C. H. Lee and F. G. Nielson, "Analysis of oscillating-water column device using a panel method," presented at the 11th International Workshop on Water Waves and Floating Bodies, Hamburg Germany, 1996.
[31] Johannes Falnes, *Ocean Waves and Oscillating Systems*. New York: Cambridge University Press, 2002.
[32] *WAMIT v6.4*. Chestnut Hill, Massachusetts: WAMIT, Inc.
[33] A. Brendmo, J. Falnes, and P. Lillebekken, "Linear modelling of oscillating water columns including viscous loss," *Appl. Ocean Res.*, vol. 18, no. 2, pp. 65–75, 1996.
[34] D. Sarkar, E. Renzi, and F. Dias, "Wave Power Extraction by an Oscillating Wave Surge Converter in Random Seas," presented at the ASME 2013 32nd International Conference on Ocean, Offshore and Arctic Engineering, Nantes, France, 2013, vol. 8, p. 5.
[35] S. K. Chakrabarti, *Hydrodynamics of Offshore Structures*. WIT Press, 1987.
[36] D. Bull and E. Johnson, "Optimal Resistive Control Strategy for a Floating OWC Device," SAND2013-6198C.

[37] R. Starzmann and V. D. Ingenieure, *Aero-Acoustic Analysis of Wells Turbines for Ocean Wave Energy Conversion*. VDI Verlag, 2012.
[38] A. Brito-Melo, L. M. C. Gato, and A. J. N. A. Sarmento, "Analysis of Wells turbine design parameters by numerical simulation of the OWC performance," *Ocean Eng.*, vol. 29, no. 12, pp. 1463–1477, Sep. 2002.
[39] M. W. L M C Gato, "An experimental investigation into the effect of rotor blade sweep on the performance of the variable-pitch Wells turbine," *Proc. Inst. Mech. Eng. Part -J. Power Energy - PROC INST MECH ENG -J POWER*, vol. 215, no. 5, pp. 611–622, 2001.
[40] C. M. Burt, X. Piao, F. Gaudi, B. Busch, and N. F. N. Taufik, "Electric motor efficiency under variable frequencies and loads," *J. Irrig. Drain. Eng.*, 2008.
[41] "Adjustable Speed Drive Part-Load Efficiency," US DOE EERE Advanced Manufacturing Office, Motor Systems Tip Sheet #11.
[42] S. Raghunathan, "The wells air turbine for wave energy conversion," *Prog. Aerosp. Sci.*, vol. 31, no. 4, pp. 335–386, 1995.
[43] T. Setoguchi and M. Takao, "Current status of self rectifying air turbines for wave energy conversion," *Energy Convers. Manag.*, vol. 47, no. 15–16, pp. 2382–2396, Sep. 2006.
[44] A. Fontaine and Smith, "Unpublished internal spreadsheet for RM6 PCC price quote. 'Revised Prices Volumes and Weights RM6 Feb 20 2014,'" Feb. 2014.
[45] T. W. Thorpe, "A Review of Wave Energy Volume 2 Appendix," Energy Technology Support Unit, United Kingdom, ETSU-R-72, Dec. 1992.
[46] A. Copping and S. H. Geerlofs, "The Contribution of Environmental Siting and Permitting Requirements to the Cost of Energy for Marine and Hydrokenetic Devices: Reference Models #1, #2, and #3.," in *Proceedings of the 9th European Wave and Tidal Conference*, Southampton, UK, 2011.
[47] A. E. Copping, S. H. Geerlofs, and L. A. Hanna, "The Contribution of Environmental Siting and Permitting Requirements to the Cost of Energy for Oscillating Water Column Wave Energy Devices: Reference Model #6.," Pacific Northwest National Laboratory, PNNL-22723, Nov. 2013.
[48] B. Polyage, A. Copping, K. Kirkendall, G. Boehlert, S. Walker, M. Weinstein, and B. Van Cleve, "Environmental Effects of Tidal Energy Development: A Scientific Workshop.," University of Washington, Seattle, Seattle, WA, USA, NMFS F/SPO-116, NOAA, Mar. 2010.

DISTRIBUTION

1 Dale Scott Jenne (electronic copy: Dale.Jenne@nrel.gov)
National Renewable Energy Laboratory
Wind and Water Power Program
15013 Denver West Parkway
Golden, CO 80401

1 Naval Architecture and Marine Engineering
University of Michigan
1221 Beal Avenue
Ann Arbor, MI 48109-2102
Attn: Dorian Brefort

3 Chris Smith, Steve Willitz, Arnold Fontaine (electronic copy: aaf1@arl.psu.edu)
Applied Research Laboratory
Pennsylvania State University
PO Box 30
State College, PA16804-0030

1 Paul Jacob
Jacob Technologies
2703 Plantation Trail
Sugar Land, TX 77478

1 Andrea Copping
Pacific Northwest National Laboratories
902 Battelle Blvd.
Richland, WA 99354

1	MS0734	Margaret Gordon	6124 (electronic copy)
1	MS1124	Diana Bull	6122 (electronic copy)
1	MS1124	Vincent Neary	6122 (electronic copy)
1	MS1124	Ann Dallman	6122 (electronic copy)
1	MS1124	Guild Copeland	6122 (electronic copy)
1	MS1135	Rich Jepsen	1534 (electronic copy)

1	MS0899	Technical Library	9536 (electronic copy)


Sandia National Laboratories